

# Aerodynamic design, simulation and test of rear wing for a Formula SAE race car

written by

Carl-Emil Grøn Christensen, s170817  
Steffan Johan Kirk, s170816

Supervisor

Jens Honoré Walther

Department of Mechanical Engineering, DTU

In fulfillment of the requirements for the degree  
of Bachelor of Science in Mechanical Engineering

# Preface

This bachelor thesis was prepared at the department of Mechanical Engineering at the technical University of Denmark in fulfillment of the requirements for acquiring a Bachelor of Science degree in Mechanical Engineering. This bachelor thesis represents the work of  $2 \times 15$  ECTS points. The work in this thesis is considered evenly distributed between both students.

The entire project is publicly available on [https://github.com/carlegroen/bachelor\\_project\\_racecar\\_aero](https://github.com/carlegroen/bachelor_project_racecar_aero), where all work files, data, various notes and CAD drawings can be found.

px

---

Carl-Emil Grøn Christensen (S170817) Date

---

Steffan Johan Kirk (S170816) Date



# Acknowledgements

We would like to thank our supervisors Jens Honore Walther and Robert Flemming Mikkelsen, for giving us the opportunity to learn intricate details about our own personal project. A special thanks to everyone on the team of Vermilion Racing, who in less than a year managed to make a dream reality. Vermilion Racing is going to compete at the Silverstone race track the 10<sup>th</sup> of July, where all of our ideas and designs are going to be tested to the limit.

The sponsors who made this project possible are all found on the following page. A big thanks goes out to everyone who supported us and assisted us in creating this project.

Thanks to Rasmus Himborg and Philips Lighting Denmark, for helping us machine a 1/4 scale wing used in the wind tunnel tests.

Thanks to Daniel Rasmussen, Bo Tranberg and Jacob Buch for assisting with graphical layout of the report.

Thanks to Nicolai Boertmann and Daniel Rasmussen for the help building the composite wings.

Thanks to DTU Skylab, and especially Martin Meister, Rasmus Bruun, Ralle Malone and Tonja Kramer for always having the time to help us when things looked most dire.

Lastly, a thank to Nenad Mijatovic. Nenad is the overall supervisor for Vermilion Racing and is a significant reason we recently became a DTU Blue Dot project - a highly prestigious title that will ensure that the team will survive for many years to come.



## Abstract

The ability to aerodynamically improve grip without adding a weight penalty is key to winning with race cars. High downforce is highly sought after, and the newly started Vermilion Racing Team at DTU is no exception. This work presents the theoretical arguments showing why downforce is important and numerical simulations to optimize the proposed rear wing dimensions. The numerical simulations are held up against a wind tunnel experiment, showing how misalignment of wings can greatly interfere with airflows, confirming the complexity of designing aerodynamical parts. The result is a design specifications of an easily producible rear wing with two elements and large end plates providing an improvement in cornering speeds between 3 – 35%, depending on the turn radius.



# Nomenclature

$\alpha$	Angle of attack
$\alpha_0$	Effective angle of attack due to airfoil camber
$\mathcal{R}$	The effective aspect ratio of the wing
$\mathcal{R}_{\text{actual}}$	The actual aspect ratio of the wing
$\ddot{x}$	Acceleration in $x$ -direction
$\delta_{\max}$	Maximum deflection distance
$\dot{x}$	Velocity in $x$ -direction
$\epsilon$	Wing tip geometry constant
$\mu$	Friction coefficient
$\nu$	Kinematic viscosity
$\rho$	Fluid Density
$\text{Eu}$	Euler number
$\text{Re}$	Reynolds number
$\text{Vol}_f\%$	Volume fraction of fiber
$A$	Frontal area or planform area
$b$	width of the wing
$c$	Chord length
$C_D$	Total drag force
$C_d$	Drag coefficient of air resistance

$C_L$	Lift coefficient
$C_l$	Lift coefficient for 2D airfoils
$C_{d_{\text{induced}}}$	Drag coefficient of induced drag
$C_{L_\alpha}$	Lift coefficient slope
$E$	Young's Modulus
$E_{\text{long}}$	Young's modulus along the direction of the fiber
$E_{\text{transverse}}$	Young's modulus in the transverse direction
$E_c$	Young's modulus of core
$E_f$	Young's modulus of fiber
$E_m$	Young's modulus of matrix
$E_{cs}$	Young's modulus of composite shell
$F_{\text{centripetal}}$	Centripetal force
$F_{\text{friction}}$	Force due to friction
$F_{\text{normal}}$	Normal force
$F_d$	Drag force
$F_L$	Lift force
$f_l$	Lift force per unit width
$F_x$	Sum of forces in $x$ direction
$g$	Force due to gravity
$h$	Height of end plate
$I$	Second moment of inertia
$L$	Characteristic length of item
$L_m$	Characteristic length of model
$m$	Mass
$P$	Motor effect

$r$  Turn radius  
 $u_\infty$  Velocity of fluid  
 $u_m$  Fluid velocity of model  
 $x$   $x$ -position  
AOA Angle of Attack  
CM Center of Mass  
PDS Product Design Specification



# Contents

1	Introduction	1
1.1	Design Philosophy	3
1.2	Problem Statement	3
2	Aerodynamic Effects on Vehicle Performance	5
2.1	Drag Effects on Straights	5
2.2	Downforce Effects on Cornering	7
2.3	Load Distribution	8
3	Airfoils and Inverted Wings	11
3.1	Airfoil theory	11
3.2	Wing Parameters	18
4	Concept Design	21
4.1	Comparison of Airfoils	21
4.2	Dimensional Requirements	23
4.3	Product Design Specification (PDS)	25
4.4	Initial Design	25
4.5	Optimization Tools	26
5	Wind Tunnel Experiment	29
5.1	Aerodynamical Theory	29
5.2	Equipment	30
5.3	Experimental Procedure	36
5.4	Results	37
6	Simulation	41
6.1	Star-CCM+	41
6.2	Mesh Generation	42
6.3	Verification of Simulation Results	43

7	Construction	51
7.1	Requirements . . . . .	51
7.2	Material Selection . . . . .	52
7.3	Composites . . . . .	52
7.4	Final Design of Rear Wing . . . . .	54
7.5	Manufacturing Final Design . . . . .	57
7.6	Final Assembly . . . . .	61
8	Discussion	63
8.1	Theory, Experiments and Simulations . . . . .	63
8.2	Product Design Specification Review . . . . .	64
8.3	Factual Improvements . . . . .	64
9	Conclusion	67
9.1	Drag Reductive System . . . . .	69
9.2	Slats, Flaps, Gills and Cutaway . . . . .	69
9.3	Suspension Integration . . . . .	69
A	Appendix	73
	Bibliography	75

# 1

## Introduction

Vermilion Racing is a newly started electric race car team at DTU building their very first vehicle: The Eevee [1]. The teams' purpose is to compete against other universities at the Silverstone race track from the 11<sup>th</sup> to the 16<sup>th</sup> of July. As members of the team, the purpose of this report is to document the design process of the rear wing of the



Figure 1.1: The teams' race car with the conceptual design of the rear wing.

## 1. Introduction

---

first car, and provide the ground works towards a full aerodynamic package for future students on the team. A render of the car's design as of the 31<sup>st</sup> of June is shown in figure 1.1. As this is the first car, this project sets out to uncover the requirements, theory and know-how behind building a rear wing.

Aerodynamics is a major decider in racing today. Cornering, not top speed is the deciding factor amongst the teams, and aerodynamics is the key. Drag, lift and side force are the three cornerstones to vehicle aerodynamics. A car's ability to handle depends on the grip of the tyres, and downforce directly increases grip by increasing the downwards load on the tyres without adding a weight penalty. Additionally, drag directly decreases the speed of a vehicle by increasing air resistance, but is of less importance as the cars of this class have far more accelerative power than the tyres can handle [2]. Designing the body-works of Eevee is therefore a dance of downforce.

This bachelor thesis attempts to lay down the ground work for designing, optimizing and manufacturing the car's rear wing. Our advisor, Jens Honore Walther, proposed simulating the wing geometry in order to both reduce financial cost and quicken the optimization process. The objective of the numerical simulations is ultimately to create an easily producable wing in a very short timespan, that produces ample amounts of negative lift for the time spent in production.

As this is the first year the team is designing and building a car, time and money for production is sparse. To validate the simulated optimizations, a wind tunnel test is performed on a down-scaled wing using Flow Similarity theory. The measurements are compared with the results from a computational fluid dynamics simulation performed in Star-CCM+ to verify the preciseness of the simulations. Based on this,  $x$ - and  $y$ -distance between the multi-element wings and angle of attack is then optimized for maximum downforce. The multi-element wing is taken from theoretical abstraction to reality by designing a physical wing. The position, deflection and dimensions of the wing is thoroughly described by the rules of the Formula Student competition, guiding the final design process. In the final chapter, theories regarding strength of sandwich-structured composites and carbon fiber molding are explained, in order to describe the design decisions. Finally, the end result is discussed and possible improvements to the wing and mounting system are listed.

Measurements and tests have been carried out at the DTU Wind laboratory's Red wind tunnel with assistance from co-supervisor Robert Flemming Mikkelsen on the 19<sup>th</sup> and 20<sup>th</sup> of June.

The entire project is publicly available on [https://github.com/carlegroen/bachelor\\_project\\_racecar\\_aero](https://github.com/carlegroen/bachelor_project_racecar_aero), where all work files, data, various notes and CAD drawings can be found. The Formula Student team at DTU: Vermilion Racing can be followed on [fb.com/FSDTU](https://fb.com/FSDTU).

## 1.1 Design Philosophy

Designing a car with hundreds, if not thousands of different factors is incredibly difficult. Therefore, determining which factors are most important for the car's performance is very crucial to the teams' success. As the timespan of this project is short, time sets a limitation on the complexity of the wing's dimension. In addition, since this is the first of its kind, no design decisions can be based on prior experience. Finally, the finances for building the car are tight. This forces us to choose a low-cost solution where basing the design on literature and the experience of competing teams is the ideal choice.

The requirements for the wing are, that it has to be as low weight as possible, in order to ensure optimum acceleration of the car. Thereto, drag has to be kept low, but the effect from drag is near negligible, which will be explained in section 2.1. Lastly, we have to maximize the downforce provided by the wing. For future iterations, ensuring that the center of pressure is kept as constant as possible is essential. If the frontwing, undertray and rear wing's downforce don't scale equally with speed, the center of pressure will move during acceleration. This will make the car's handling unpredictable, and potentially limit the driver's confidence in the car.

## 1.2 Problem Statement

A new aerodynamically beneficial structure is to be implemented at the rear of the Eevee with the purpose of increasing the tyre's grip without adding a weight penalty. The goal is to have a cheap, both time- and money-wise, rear wing, which provides enough negative lift to benefit the car's lap time.



# 2

## Aerodynamic Effects on Vehicle Performance

The first argument to the importance of aerodynamics is based on two facts: The fact that drag is negligible in regards to the Formula Student vehicle's top speed on straights, and the fact that aerodynamically increasing the vehicle's effective mass due to downforce increases tyre grip, which in turn allows for higher cornering velocities.

The second part of this chapter covers the importance of centering the effective mass increase due to aerodynamic devices close to the center of gravity – otherwise handling characteristics becomes a function of velocity.

### 2.1 Drag Effects on Straights

First, let's explain what makes a car fast, and what parameters we can change to improve the speed of our car. The car's acceleration can be described by Newton's second law as:

$$\sum F_x = ma \tag{2.1}$$

## 2.1. Drag Effects on Straights

---



Figure 2.1: Frontal area of the car with a dummy wing inserted into the CAD model, in order to get an estimate of the drag coefficient  $C_D$ .

Where the sum of forces working in the x-direction (the direction of travel) can be expressed as the force already pertained by the vehicle: The force the motor exerts is given by  $F = \frac{P}{\dot{x}}$ , where  $P$  is the power of the car, minus the drag force:

$$F_D = \frac{1}{2} C_D \rho \dot{x}^2 A \quad (2.2)$$

$$F_{\text{motor}} = m \ddot{x} = \frac{P}{\dot{x}} \quad (2.3)$$

$$\sum F_x = F_{\text{motor}} - F_D = \frac{P}{\dot{x}} - C_D \left( \frac{1}{2} \rho \dot{x}^2 A \right) = 0 \quad (2.4)$$

Where  $C_D$  is the drag coefficient of the vehicle,  $\rho$  is the density of the fluid it moves in and  $A$  is frontal area of the vehicle. Solving for maximum speed, that is, when the two forces sum to zero:

$$F_{\text{motor}} = F_D \quad (2.5)$$

As we were interested in the max speed of the car, let's solve for the velocity, giving:

$$\dot{x} = \left( \frac{2P}{C_D (\rho A)} \right)^{\frac{1}{3}} \quad (2.6)$$

This is assuming we're traveling at terminal velocity – that is, the point where the Driving Force = Friction Force. The terminal velocity of the racer is then easily calculated, as the competition restricts the maximum amount of power to 80 kW, and the frontal area of the car is approximated from the CAD drawing seen in figure 2.1.

$$\dot{x}_{\max} = \left( \frac{2 \cdot 80 \text{ kW}}{0.85 (1.225 \text{ kg m}^3 \cdot 0.99 \text{ m}^2)} \right)^{\frac{1}{3}} = 53.7 \text{ m s}^{-1} = 193.5 \text{ km h}^{-1} \quad (2.7)$$

however, given the ruleset a forecasted maximum of 110 km h<sup>1</sup> allows a much larger drag coefficient  $C_D$ :

$$C_D = \frac{2P}{\dot{x}^3 (\rho A)} = \frac{2 \cdot 80 \text{ kW}}{(110 \text{ km h}^{-1})^3 (1.225 \text{ kg m}^3 \cdot 0.99 \text{ m}^2)} = 4.62 \quad (2.8)$$

Thus, the car's top speed will only be limited by a drag factor > 4.62, which is far above the drag introduced by the aerodynamic devices.

From this derivation, it is clear that the car's abilities at maximum speeds far exceed the requirement of the track. Therefore, the next step is to improve cornering speeds which depend strongly on the tyre's grip on the surface of the road [2].

## 2.2 Downforce Effects on Cornering

Shown before, drag does not limit the car's performance on straights. During cornering, drag is not an issue either, but the grip of the tyres limits the maximum velocity before the vehicle loses traction due to the centripetal force which is given by: [3]

$$F_{\text{centripetal}} = \frac{m\dot{x}^2}{r} \quad (2.9)$$

where  $r$  is the distance to the center of the cornering circle. The frictional force the car exerts due to downforce and tyre grip is given by:

$$F_{\text{friction}} = \mu F_{\text{normal}} \quad (2.10)$$

### 2.3. Load Distribution

---

where the normal force is given by both the weight and (negative) lift of the car, which serves as an effective mass increase:

$$F_L = \frac{1}{2} C_L \rho A \dot{x}^2 \quad (2.11)$$

$$F_{\text{friction}} = \mu \left( mg + \frac{1}{2} C_L \rho A \dot{x}^2 \right) \quad (2.12)$$

The vehicle will lose traction when the frictional force is less than the centripetal force.

$$\frac{m \dot{x}^2}{r} > \mu \left( mg + \frac{1}{2} C_L \rho A \dot{x}^2 \right) \quad (2.13)$$

Giving the maximum velocity for a given corner radius before the car skids out:

$$\Rightarrow \dot{x} < \left( \frac{2\mu m g r}{m - \mu C_L \rho r A} \right)^{\frac{1}{2}} \quad (2.14)$$

Again, the forecasted variation in radii of corners is prescribed by the rules to be between 3 m to 50 m [4]. Plotting this for various  $C_L$  values between 1.5 to 2.6 [5], assuming  $m = 300$  kg,  $\mu = 1.5$  [6] and  $A = 0.99$  m<sup>2</sup> as previously used. The result can be seen in figure 2.2.

## 2.3 Load Distribution

The scope of this thesis is not to incorporate a full aerodynamic package, but a quick overview of load distribution is essential to understanding the behaviour of the car.

The effective mass added from negative lift depends on the lift coefficient. It is evident that different items on the car carry different lift coefficients, thus making the lifting forces over the cars length a function of relative speed. For the unexperienced driver, this is not easily managed as handling characteristics change with velocity. Therefore, it is desirable to have the aerodynamic center of pressure close to the car's center of gravity, in order to have similar handling at all velocities. While this is not handled in this thesis, it is ideal for future iterations and essential for a full aerodynamical package.

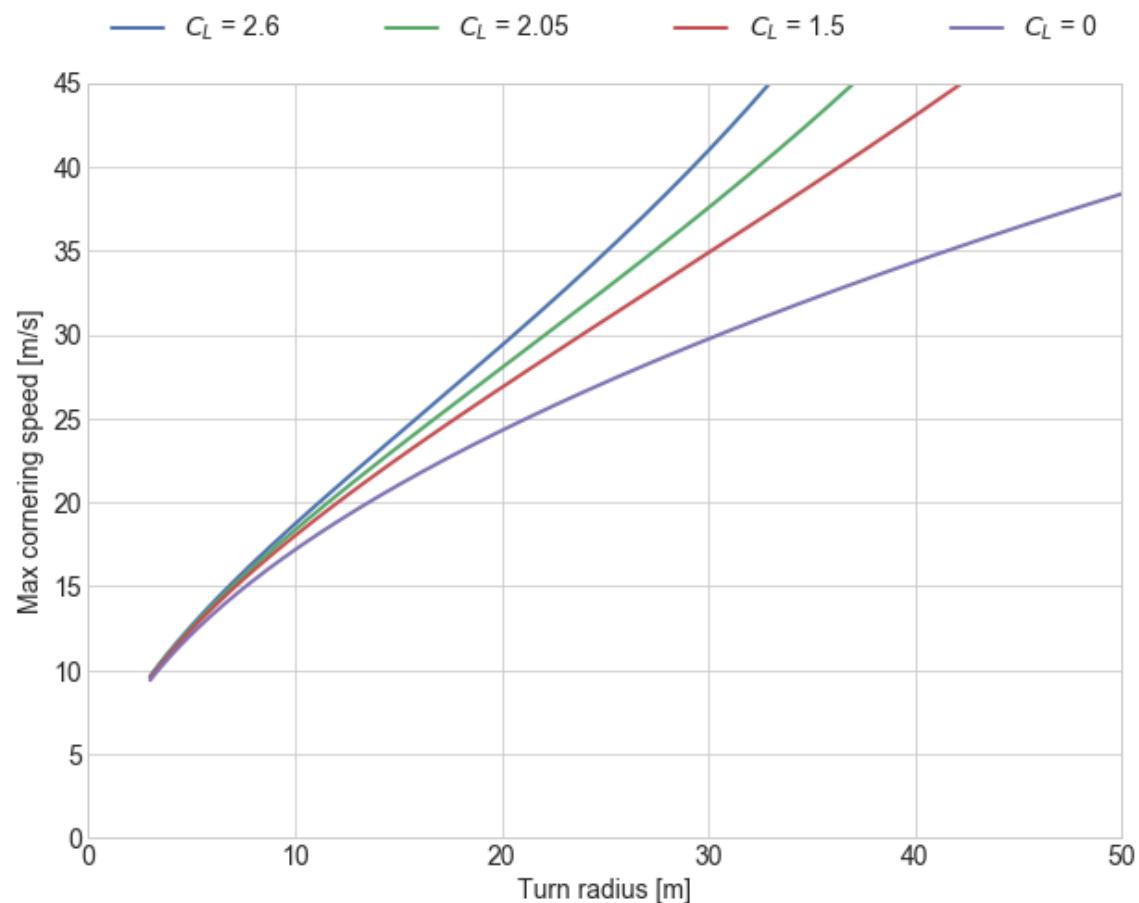


Figure 2.2: Cornering speed as a function of turn radius for various lift coefficients.



# 3

## Airfoils and Inverted Wings

Achieving a large negative lift coefficient  $C_L$  can be done in many ways. Inspecting race cars throughout the years show that airfoils have been used as early as 1966 when Jim Hall attached a rear wing to his Chaparral 2E [7]. Since then, the inverted wings have been a staple in the racing industry with various three dimensional geometries affecting the overall performance even further.

This chapter covers the pressure distribution of various airfoils, the selection criterions of the competition, three dimensional geometrical effects and the tools of the optimization trade.

### 3.1 Airfoil theory

An airfoil is the 2-dimensional cross section of a wing, that is defining of the wing's lifting characteristics. It is important to know the nomenclature, which is shown on figure 3.1: The leading edge is the most forward point of the wing, the trailing edge is the most rearward point of the wing. Camber is how much the wing bends.

When an airfoil moves in a fluid, the streamlines of the particles move as seen in figure 3.2. The streamline stops at the stagnation point, which is usually the leading edge. The other can be divided into two categories, as the flow can only go to two places: The suction surface and the pressure surface.

The suction surface is the surface where the flow accelerates to high

### 3.1. Airfoil theory

---

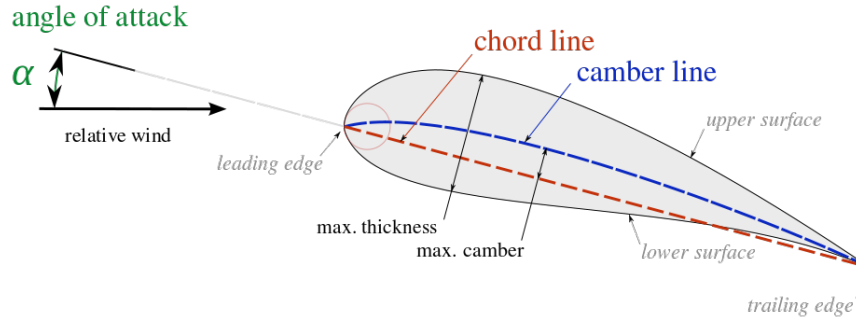


Figure 3.1: Figure explaining angle of attack, chord line, camber line, upper surface (suction surface), lower surface (pressure side), leading edge and trailing edge. Figure taken from [8].

velocities and the pressure drops. This can be seen on the top part of figure 3.2, where the corresponding pressure distribution can be seen below as the (-) part. A peak of very low pressure can be found near the leading edge, which is often called the suction peak.

The pressure surface is the surface where the flow decelerates to lower velocities and the pressure increases. This is the bottom part of 3.2, which provides a much lower force from the pressure than the suction side.

The resulting changes in pressure forces the wing upwards, creating lift. It is important to note, that the suction side contributes considerably more to lift in most cases [2].

#### 3.1.1 Airfoil Lift and How to Increase it

Increasing the lifting capabilities of an airfoil can be done in several ways.

First, the angle of attack of an airfoil usually increases lifting characteristics of a wing, until reaching a certain threshold where it falls off. An airfoil carries its lifting abilities usually while flow is attached - that is, where the streamlines follow the shape of the airfoil. If the flow separates from the surface of the airfoil, the lift behaviour becomes unpredictable. This effect is called stalling.

There are two types of stalling: Leading edge separation which are quite abrupt and greatly decreases lift, and trailing edge separation,

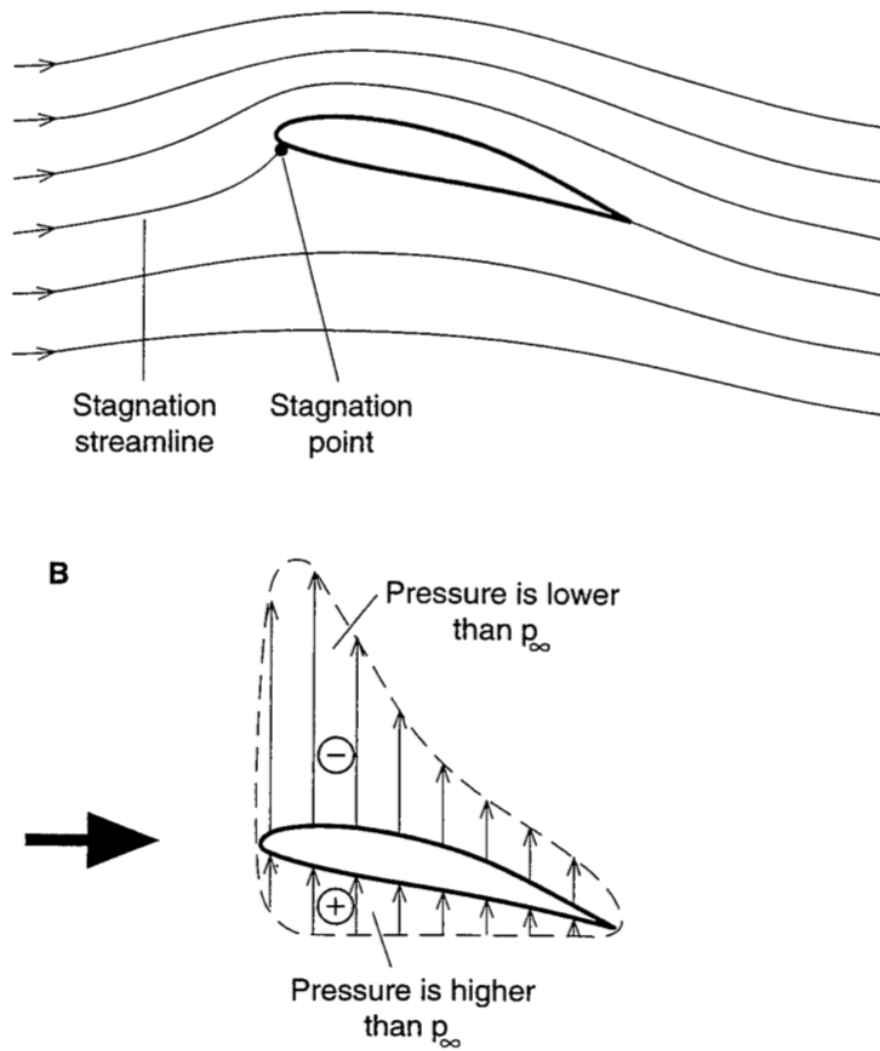


Figure 3.2: A figure showing the streamlines around a slightly cambered airfoil, along with its pressure distribution below. Figure taken from [2].

### 3.1. Airfoil theory

---

which gradually reduces the lift. These are called a hard and soft stall, respectively. Thus, a soft stall is preferred in racing, as a hard stall will instantly change the car's handling abilities.

Secondly, another way of changing the lift is by creating an effective change in angle of attack: Changing the wing's camber. The trailing edge of an airfoil's camber-line is the largest contributor to lift. By changing the camber geometry, the lift can be changed greatly, and the largest increase is found in the trailing edge region. This is why the introduction of flaps is prominent in both aircraft and race car wings.

Lastly, the thickness of the airfoil affects lift up to a certain point, and the optimum thickness is about 12% of the camber length. For the interested reader, reference [2] explores this further.

#### 3.1.2 Reynolds Number, Lift and Drag Coefficient

The Reynolds number is an dimensionless number that is used to predict the flow of fluids in different flow configurations. In general the Reynolds number is used to predict if a flow is laminar or turbulent. The Reynolds number is defined as:

$$Re \equiv \frac{u_\infty L}{\nu}, \quad (3.1)$$

where  $u_\infty$  is the velocity of the fluid,  $L$  is a characteristic length, for an airfoil this would typically be the chord length, and  $\nu$  is the kinematic viscosity of the fluid.

$$(3.2)$$

The usage of Reynolds number when designing an airfoil is the fact that the flow is similar for different scales of the same model if the Reynolds number is the same. Thereby a smaller model can be built and tested at a higher velocity than the full scale, thereby amounting to the same Reynolds number and fluid flow characteristics.

The lift coefficient is a dimensionless coefficient that relates the lift generated to the fluid the airfoil moves in, the velocity of the fluid and the reference area. This coefficient is defined as:

$$C_l \equiv \frac{F_l}{\frac{1}{2} \rho u_\infty^2 c} \quad (3.3)$$

Where  $F_l$  is the lift per unit width,  $\rho$  is the density of the fluid,  $x_\infty$  is the velocity of the surrounding fluid and  $c$  is the chord length. For a specific wing, that is, where an airfoil has a physical extension, the lift coefficient is defined as:

$$C_L \equiv \frac{F_L}{\frac{1}{2} \rho u_\infty^2 A} \quad (3.4)$$

Where  $F_L$  is the total lift force, and  $A$  is the surface area. For a wing with both camber and angle of attack,  $C_L$  is found by the following formula:

$$C_{L0} = C_{L_\alpha}(\alpha + \alpha_{L_0}) \quad (3.5)$$

where  $\alpha$  is the lift per angle of attack in radians,  $\alpha_{L_0}$  is the airfoil's camber, which acts as a additional angle of attack effect, also in radians.  $C_{L_\alpha}$  is given by: [9]

$$C_{L_\alpha} = \frac{2\pi}{1 + \frac{2}{AR}} \quad (3.6)$$

However, it is important to note that equation 3.6 is derived for elliptical wings and is thus an approximation [10]. A correction of the lift due to downwash effects is found in the section below.

Like lift, a dimensionless drag coefficient exist, that describes how drag is generated in a similar fashion:

$$C_d \equiv \frac{2F_d}{\rho u^2 A} \quad (3.7)$$

Where  $F_d$  is the drag force - the component of the force that is parallel with the flow velocity [11]. The induced drag created by the lifting force must also be added in order to find the total drag coefficient [12]:

$$C_D = C_d + C_{d_{\text{induced}}} \quad (3.8)$$

where  $C_{d_{\text{induced}}}$  is given by:

$$C_{d_{\text{induced}}} = \frac{C_L^2}{\epsilon \pi AR} \quad (3.9)$$

The derivation and explanation hereof is found in the section below.

### 3.1. Airfoil theory

---



Figure 3.3: The trailing tip vortex is clearly seen to the right. Thanks to the NASA's Wake Vortex Study for the photo [13].

#### 3.1.3 Aspect Ratio and End Plates

An important identifier when describing an actual finite wing is, apart from chord length and airfoil design, the width. The definition used for describing the physical span is called Aspect Ratio, and for a rectangular wing is:

$$AR_{\text{actual}} = \frac{b}{c} \quad (3.10)$$

Where  $b$  is the width of the wing and  $c$  is the chord length.

The effect of having a finite length is very important in race aerodynamics. As pressure is lowered and increased on the different sides, air is going to travel around the edge of the wing in a rolling motion. This creates a vortex, which is shown in figure 3.3. The phenomenon is called tip vortices, and the magnitude of the vortex is proportional to the lift coefficient of the wing. The area these vortices cover is very large and for wings with a small span will greatly reduces the lifting powers.

These vortices are created by an effect called downwash when talking aeroplanes. As the wing bends the air slightly downwards, it creates an opposite force due to Newton's second law: Lift. However, the sheet of air that passes over the length of the wing has a downward velocity component and will thus force air in that direction. This presses other air out of the way, allowing air above it to rush downwards to fill the gap. The same phenomenon is what happens at the edge of the wing, and again is what is shown in figure 3.3. When the wing bends the airflow downward, drag is induced. While drag is almost negligible in our case, it is never wanted [14]. For an elliptical wing, the induced drag coefficient is given by:

$$C_{d\text{induced}} = \frac{C_L^2}{\epsilon \pi A} \quad (3.11)$$

Where  $\epsilon = 1$  for an ellipse, and generally  $\epsilon < 1$  for anything else. For a rectangular wing,  $\epsilon = 0.7$  [12].

For a small aspect ratio wing, the lift coefficient has to be scaled down due to the effect of downwash.

$$C_L = \frac{C_{L0}}{1 + \frac{C_{L0}}{\pi A}} \quad (3.12)$$

Where  $C_{L0}$  is the lift for a thin flat plate, as given in equation 3.5 and  $A$  is the wing's aspect ratio [15].

$$(3.13)$$

A way to combat this lift-reducing phenomenon is the addition of end plates. End plates adds a virtual additional length by adding a physical wall between the low- and high pressure surfaces. The vortices that usually go around the wing and reduce lift is severely hindered. A corrected aspect ratio can be found for wings with side plates as:

$$A' = A_{\text{actual}} \left( 1 + 1.9 \frac{h}{b} \right) \quad (3.14)$$

where  $h$  is the height of the end plate, and  $b$  is the width of the wing as in equation 3.10 [2]. The addition of end plates gives an increased aspect ratio. Inserting this back into 3.12 shows that end plates yields an increase in lift.

### 3.2. Wing Parameters

---

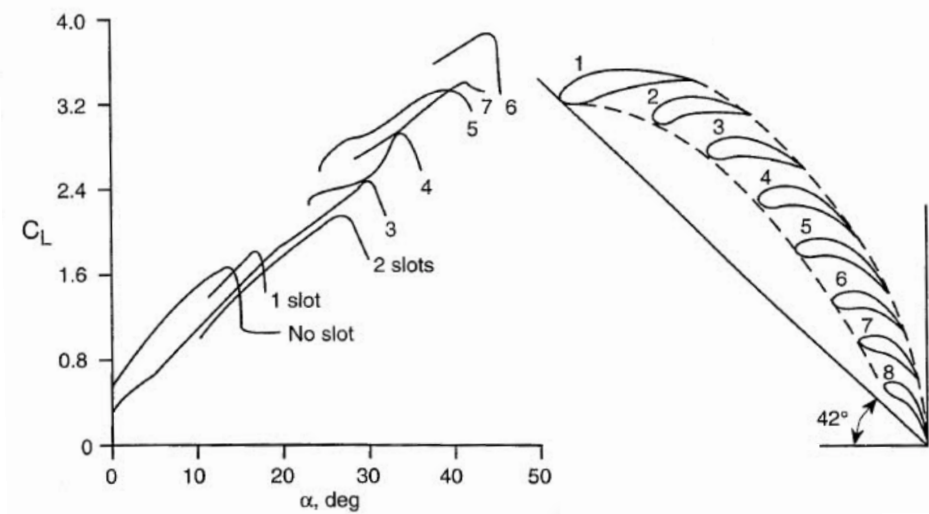


Figure 3.4: Lift coefficient as a function of effective angle of attack. The No slot line corresponds to a single element wing, and the 1 slot corresponds to a double element wing. Figure taken from [2].

#### 3.1.4 Multiple Elements and Maximum Downforce

As mentioned before, in order to increase downforce on a wing (made of a predefined airfoil) there are two options: Increasing the width of the wing, or increasing the camber. As the width is fixed by regulations, the camber has to be varied. Increasing camber usually causes flow separation, but by splitting the airfoil into multiple elements, this can be circumvented while gaining effective airfoil camber. The camber attained by using multiple elements is usually much higher than with a single element, and letting the high pressure from the first element transition to the low pressure zone of the secondary element results in a favorable interaction between the two elements.

The lift coefficient can be seen as a function of (effective) angle of attack in figure 3.4. Notice how the combined camber can be increased before stalling occurs and lift increases. A leading airfoil (also called a slat) will extend the range of possible camber even further, but will not increase the lift curve [2].

## 3.2 Wing Parameters

The previous sections describe which parameters can be varied in order to attain better aerodynamical properties, such as higher lift, robust-

### 3.2. Wing Parameters

---

Parameter	Effect	Optimization Technique
Thickness	Usually predefined by airfoil	N/A
Angle of Attack	Changes lift characteristics	Finding the optimum angle of attack
Camber	Usually predefined by airfoil	Adding additional Elements
Position between elements	Changes lift characteristics	Optimizing $x, y$ position between elements
Size	Sizes directly increases lift	Finding the maximum allowed size by regulations

Table 3.1: Table of parameters that can vary and how to optimize the parameter.

ness towards stall and protection against trailing tip vortices. Improving a wing has several optimization parameters and in table 3.1 is a list of how these are going to be handled in the following sections.



# 4

## Concept Design

The following contains the conceptual design of a rear wing based on the previous chapters. First, a walkthrough of different airfoil profiles and their benefits is followed by selection of one particular. Second, analyzing the amount of elements the wing should consist of with regards to production time and ease of construction. Third, the dimensional requirements outlined by the competition rules are given, and finally, a Product Design Specification (PDS) is set up to make sure that the design solution addresses all the problems it attempts to solve. Based on the PDS, an initial design is proposed, followed by a section describing the various possible methods of optimization.

### 4.1 Comparison of Airfoils

Finding a fitting airfoil requires deep investigation of airfoil databases and articles. The requirements for this airfoil according to the PDS is a really high lift wing, operating at large ranges of Reynolds numbers, where the highest (according to track regulations) is around:

$$Re = \frac{uL}{\nu} = \frac{30.56 \text{ m s}^1 \cdot 0.6 \text{ m}}{1.491 \times 10^5 \text{ m}^2 \text{ s}^{-1}} \approx 1.2 \times 10^6 \quad (4.1)$$

to around:

$$Re \approx 3 \times 10^5 \text{ at } 15 \text{ m s}^1 \quad (4.2)$$

which is the speed estimated for the tightest corners in the competition [4]. Thereto, the airfoil should have soft stall characteristics and

#### 4.1. Comparison of Airfoils

---

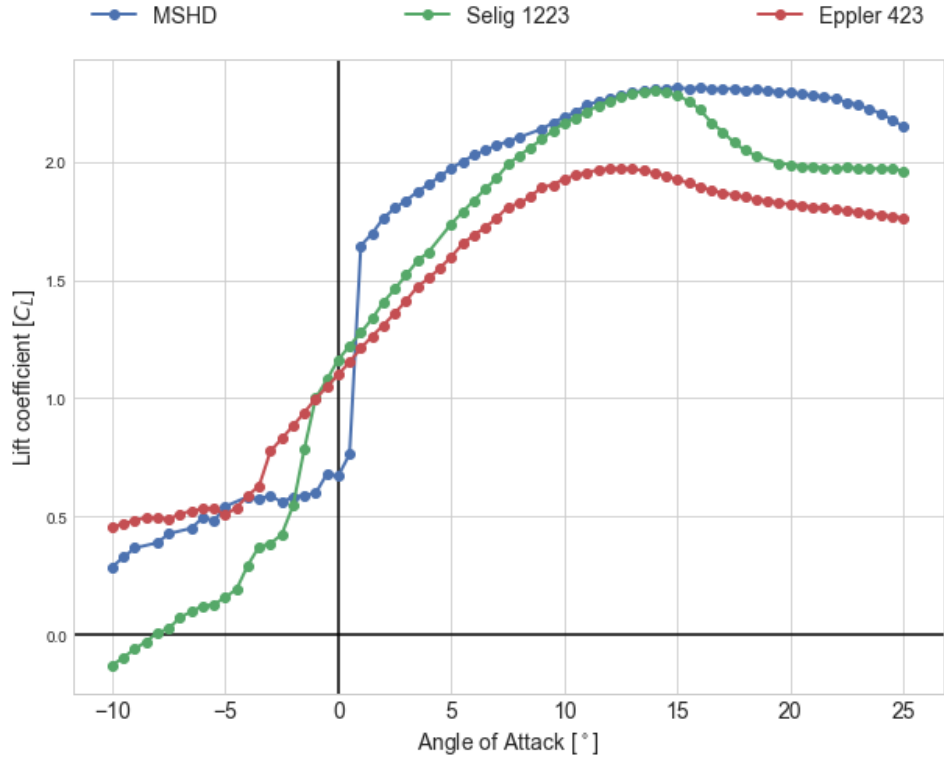


Figure 4.1: A comparison of the three airfoils as a function of angle of attack. The MSHD profile shows high lifting characteristics over a wide range of angles of attack. Comparisons are from XFOIL at  $\text{Re} = 3 \times 10^5$ .

be very resilient to laminar separation bubbles (LSB for short. The interested reader is referred to reference [2]). This is done by having a large leading edge radius. The Reynolds number is an

After a thorough research comparing high lift-low Reynolds number airfoils functioning over a wide variety of angles of attack, three airfoils are selected for further examination. The Eppler E423, the Motor Sport High Downforce (MSHD) and finally the Selig S1223. The lift coefficients can be seen as a function of angle of attack in figure 4.1.

The MSHD performs incredibly well over a wide range of AOAs, with very low variation in lift coefficients. The MSHD airfoil is designed specifically for the Formula Student competition, which does make the choice rather obvious. The MSHD is selected for further investigation, and will be the airfoil of choice.

Finding the right amount of elements depends on the airfoil, and based on the MSHD profile and previous studies, two elements were chosen: A

main element and a scaled down flap with 35% of the length of the main element [16]. The two elements will have an identical airfoil, as this is a classical way of generating successful multi element wings [17]. This makes production time shorter, monetary cost lower and (hopefully) provides ample lift for the first generation race car.

## 4.2 Dimensional Requirements

The formula student competition has a clear ruleset dictating the dimensional requirements of aerodynamic devices. The most crucial elements are outlined below:

Height Restrictions:

T7.3.1 All aerodynamic devices rearward of a vertical plane through the rearmost portion of the front face of the driver head restraint support, excluding any padding, set to its most rearward position must be lower than 1.2 m from the ground.

Width Restrictions:

T7.3.2 All aerodynamic devices higher than 500 mm from the ground, must not extend outboard of the most inboard point of the rear wheel/tire.

Length Restrictions:

T7.3.3 All aerodynamic devices must not extend further rearward than 250 mm from the rearmost part of the rear tires

Minimum Edge Radii of Aerodynamic Devices:

T7.4 All forward facing edges of aerodynamic devices that could contact a pedestrian must have a minimum radius of 5 mm for all horizontal edges and 3 mm for vertical edges.

Rules from Formula Student UK 2018 ruleset [4].

The dimensional requirements from the rules was sketched on the front plane of the car's CAD drawing. This allows positioning the wing in the square seen in figure 4.2.

#### 4.2. Dimensional Requirements

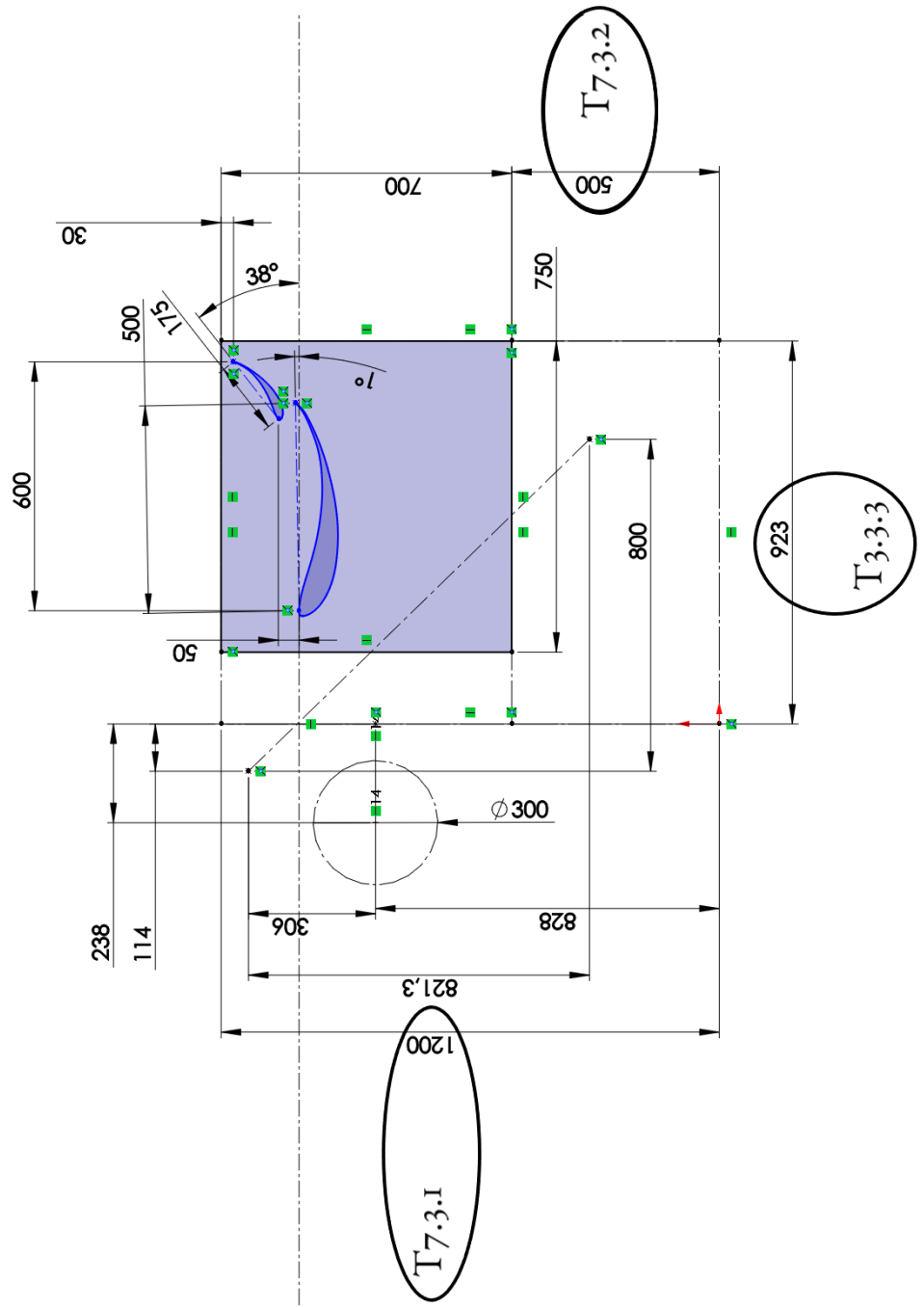


Figure 4.2: The ruleset above drawn against the design of the car. The marked square is the area where the wing can be freely placed.

### 4.3. Product Design Specification (PDS)

Issue	Requirement	Criteria
Weight	Must not move CM above halfway point	As low as possible
Safety	Must be in compliance with FSAE rules	Should not make handling difficult for driver
Durability	Must have no fatigue limit. Must be waterproof	
Performance	Must have high downforce & soft stall characteristic at all speeds	Should retain performance despite tripping. Should have end plates.
Dimensioning	Must be within area defined by FSAE rules	Should allow space for motor removal.
Production	Must have low time- and monetary cost	

Table 4.1: The PDS table shows how the final design lives up to the proposed specifications.

## 4.3 Product Design Specification (PDS)

The PDS is a design tool created to ensure that the project solves the problems it set out to. The specifications uncovered in the previous sections are boiled down to their bare essentials, and in order to cover as large a solution space as possible, the PDS contains as few requirements as possible. However, fulfilling the requirements is essential for a proper solution. While the criteria are not crucial, implementing the criteria are the difference between an acceptable solution and a good one. The PDS will be revised at the discussion section, in order to verify the design solution fulfills all requirements.

## 4.4 Initial Design

An initial design can be made based on the PDS and the design ideas above. The MSHD airfoil has a lot of the wanted characteristics: High downforce, both leading- and trailing edge stalls are soft, and the usable AOA-ranges are high. Furthermore, based on equation 3.14, we want as large end plates as possible, which will therefore fill the en-

## 4.5. Optimization Tools

---

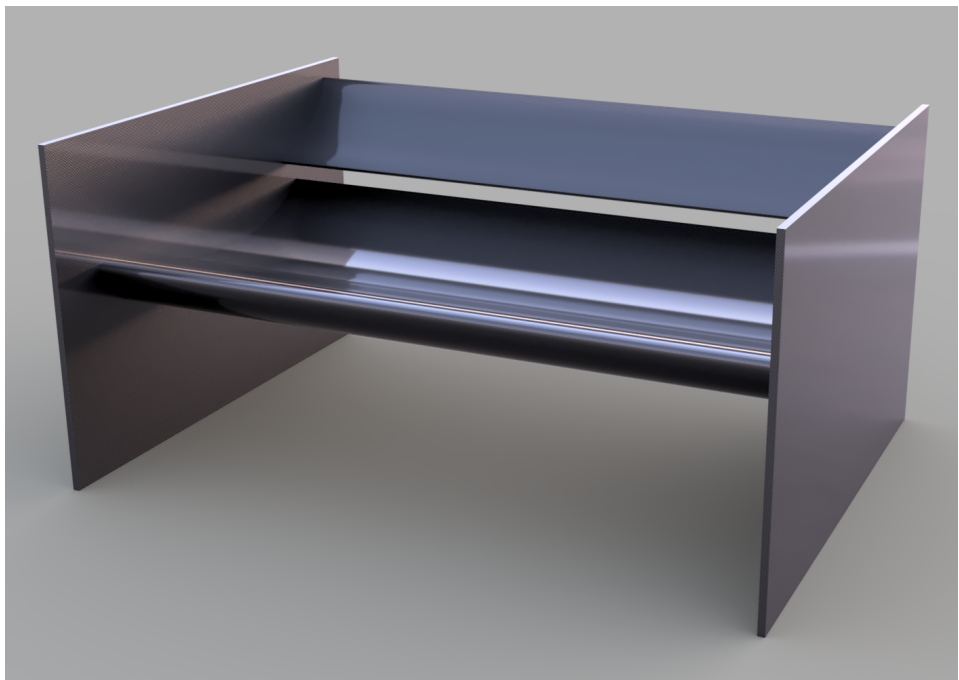


Figure 4.3: Initial design of the rear wing based on the PDS and initial research. Optimization of the wing is the next step.

tirety of the allowed area. The dimensional requirements from the FSUK rules dictate the maximum width, as shown in figure 4.2. Finally, two elements are chosen as that gives a large amount of lift over even higher angles of attack, while being cheap timewise to construct, as seen in figure 3.4

A first draft of the design can be seen in 4.3. As the wing is intended to be optimized, a few initial assumptions were made. The first element's tail is angled  $1^\circ$  below horizontal, and the angle between the two wing elements is  $38^\circ$  based on a previous study [16]. The same article provides a first guess of the relative size of the two elements.

## 4.5 Optimization Tools

In order to optimize a wing design, there are usually three ways employed in aerodynamics.

Road testing might seem the easiest method of testing, but constructing full-scale rear wing and iterating is very time consuming. Furthermore, in order to measure downforce correctly, suspension vibration, varying weather and such have to be taken into account, and as this

is the first car that's being produced, there is no car to test on. The unprofessional driver performance is also rarely repeatable, thus making actual road testing a time consuming and inaccurate method of testing the wings.

Wind tunnels is another option. This allows for construction of down-scaled models, as long as Reynolds numbers are scaled accordingly. However, models can also be difficult to produce, and might not reproduce full scale results correctly. Full scale testing is expensive and wind tunnels of that size are rare.

Lastly, computational fluid dynamics offer a method of testing a wing without actually producing anything physically. Albeit the seemingly great possibilities, computer time is also expensive, and high resolution solutions require very powerful computers [2]. Luckily for us, we have access to the Nifheim Linux supercomputer cluster located at the Department of Physics at the Technical University of Denmark. The supercomputer has a total of 11368 CPU cores, with 235 Teraflops of processing power.

In order to verify the numerical models applied to the problem, a wind tunnel test will be performed on a 1/4 scale model and be compared to simulations. Post verification, numerical optimization of the wing will follow in Star-CCM+.



# 5

## Wind Tunnel Experiment

Verifying the simulated aerodynamic effects is imperative to verify the numerical analysis. In order to assess the reliability of the previously mentioned simulations, a physical measurement of the pressure along the down-scaled wing will provide results for comparison. When conducting tests on models, knowing how the flow behaves on different length scales and at different velocities is a requirement. Accordingly, this chapter starts with discussing the fluid theory behind the experimental setup.

Measurements and tests have been carried out at the DTU Wind laboratory's Red wind tunnel with the help of our supervisor Robert Flemming Mikkelsen the 19<sup>th</sup> to the 20<sup>th</sup> of June.

### 5.1 Aerodynamical Theory

The theories explaining how fluid effects scale between varying wing sizes is explained, in order to justify using a down-scaled model as evaluation to a real size wing.

#### 5.1.1 Similarity of Flows

In order to perform tests on the rear wing, it has to be scaled down to fit inside the wind tunnel. This reduces the physical size of the wing, which under equal circumstances changes the flow around it. In order to correctly emulate the simulated flow inside a wind tunnel, the

## 5.2. Equipment

---

Reynolds number of the full scale flow and the model scale flow has to be the same.

$$Re_m = Re \quad (5.1)$$

Mathematically, the Reynolds number are defined as:

$$Re = \frac{uL}{\nu} \quad (5.2)$$

where  $u_\infty$  is the velocity of the fluid in motion,  $L$  is the characteristic length and  $\nu$  is the kinematic viscosity of the fluid.

For a down-scaled model, matching Reynolds number requires an increase in velocity, inversely proportional to the increase in length:

$$\begin{aligned} \frac{u_m L_m}{\nu} &= \frac{uL}{\nu} \\ \Rightarrow u_m &= \frac{L}{L_m} u \end{aligned} \quad (5.3)$$

Given the nature of the competition, the average cornering speeds are around  $55 \text{ km h}^{-1} = 15.28 \text{ m s}^{-1}$ , which is where downforce is of most importance. The desired velocity in the wind tunnel for the scale model can be found from equation 5.3:

$$u_m = \frac{0.6 \text{ m}}{0.15 \text{ m}} 15.28 \text{ m s}^{-1} = 61.12 \text{ m s}^{-1}$$

Which in accordance to the range of the Red wind tunnel.

## 5.2 Equipment

The equipment required for performing a wind tunnel test can be seen below:

- The Red wind tunnel ( $60 \text{ m s}^{-1}$  to  $65 \text{ m s}^{-1}$ )
- 1/4 scale wing
- Syringe inserts for pressure taps
- Rubber tubing
- Strain gauge for lift

The instrumentation and the Red wind tunnel is described below, along with a thorough description of the scale wing designed and produced for the experiment.



Figure 5.1: Robert Mikkelsen posing in front of the Red wind tunnel. To the left is the air inlet, followed by the test section.

### 5.2.1 Instrumentation

Instrumentation to perform the experiments were graciously provided to us by DTU Wind Energy. The following contains a description of the wind tunnel, data-logging devices and software used to perform the measurements.

#### The Red Wind Tunnel

The red wind tunnel is an open loop wind tunnel located at DTU Lyngby. A picture of the wind tunnel with our supervisor Robert Mikkelsen can be seen in figure 5.1. It measures  $0.5\text{ m} \times 0.5\text{ m} \times 1.3\text{ m}$  in the test section, with a maximum wind speed of  $65\text{ m s}^{-1}$ . The wind tunnel functions in low Reynolds number, which fits with the chosen MSHD aerofoil.

#### Pressure Measurements

The Red wind tunnel is equipped with data logging equipment measuring up to 64 pressure probes on a wing profile, the Angle of Attack (AOA), a force gauge measuring the lift forces, a pitot rake measuring the pressure in the wing's wake, the dynamic pressure in the wind tun-

## 5.2. Equipment

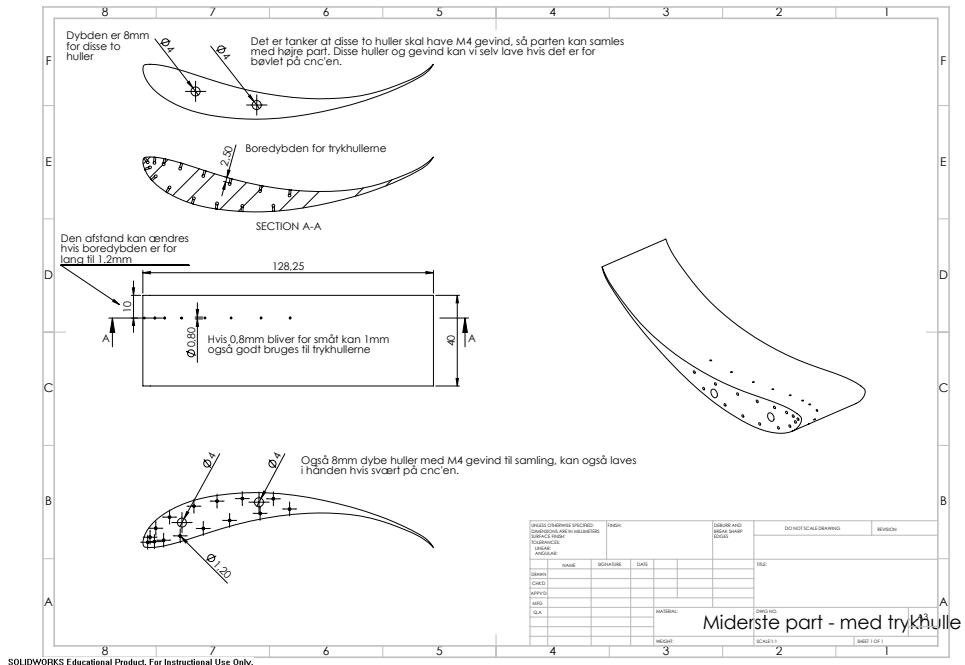


Figure 5.2: Blueprints of the centrepiece of the wing containing the pressure taps for generating a pressure distribution profile.

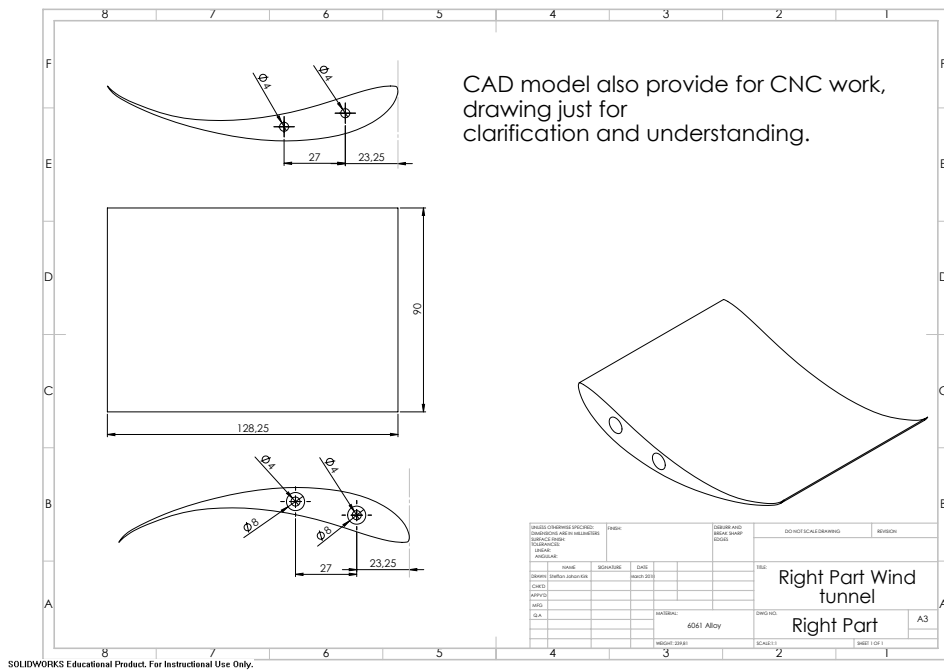
nel, the operational speed of the wind tunnel, the air density and the time of measurement. The measurement equipment was connected to the data-logging software LabVIEW on a nearby computer.

### 5.2.2 Manufacturing the 1/4 Scale Rear Wing

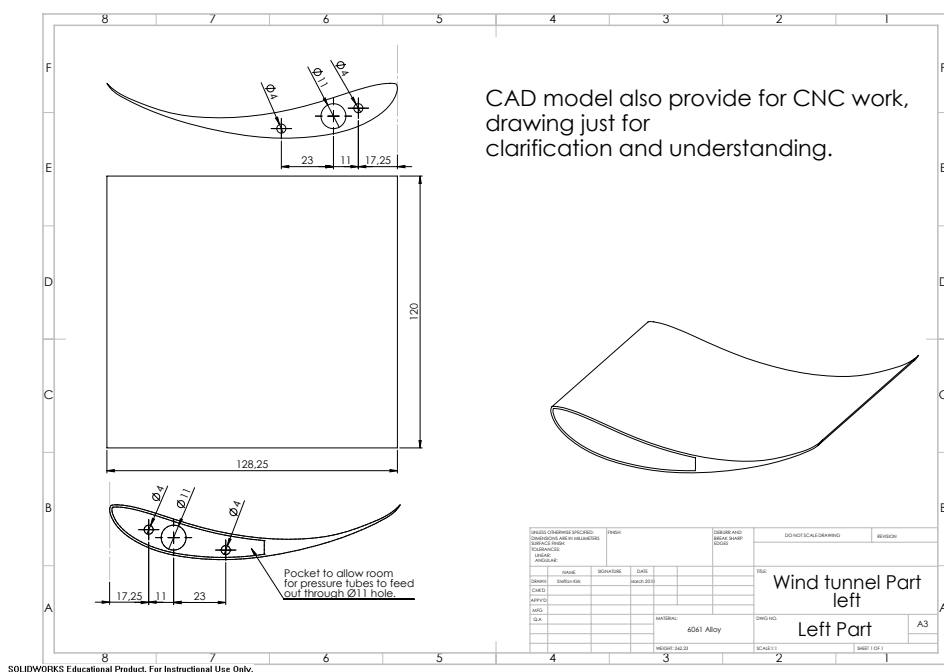
When producing the small scale model, obstruction of the total area has to be taken into account. The blockage ratio is optimally below 5%, with up to 10% compensation. Problematically, getting pressure outlets out of a very small wing is very difficult, and drilling pressure taps along the leading edge also proves to be tedious if made too small. Therefore, a quarter scale wing was chosen with a frontal area of 0.013 75 m<sup>2</sup>. Given the tunnel area of 0.25 m<sup>2</sup>, that gives us a blockage ratio of 5.5% - just slightly above the recommended obstruction ratio.

After the initial analysis of airfoils, this design was chosen based on preliminary research. From [16], a rule of thumb for multi element design is that the first element should be around 70% of the total chord length, and the second element around 30%. From [2], the initial position of the elements was chosen. Having the perfect position is not essential, as the experiment is a simply a verification method of the

## 5.2. Equipment



(a) Blueprints of the right section of the wing.



(b) Blueprints of the left section of the wing with a pocket allowing pressure tubes to be fed through. Additionally fitted with an  $\varnothing 8$  mm H7 hole for mounting the wing vertically.

## 5.2. Equipment

---

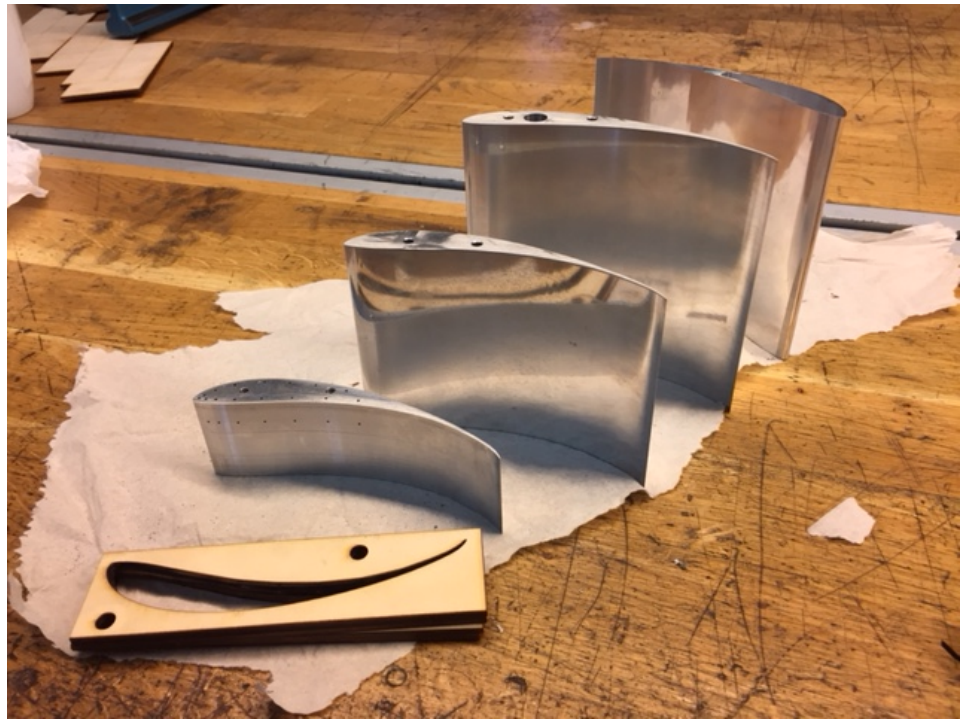


Figure 5.4: Pieces of the downscaled wing before assembly. Additional H7 holes had to be drilled in order to mount the wing to the force gauge securely.

computational method, which will be used to optimize the final design. The 1/4 scale rear wing was machined at Philips Lighting by Rasmus Himborg based on the technical drawings presented in the following section.

### Blueprints

The wing requires a series of pressure taps for the measurements needed. 15 holes have to be made along the very narrow wing profile to measure the pressure on the wing's surface. The pressure taps have to be  $\phi 0.8$  mm on the outside, with an inner bore hole with  $\phi 1.2$  mm to have a syringe inserted. The wing needs to be separated into smaller parts, as drilling  $\phi 1.2$  mm pressure inlets throughout the entire wing is very difficult. Thus, the large wing is dissected into three parts. A central part with 15 pressure taps, and two regular wings with holes for pressure tubes to escape. The left section contains a H7 hole for fitting the wing in the wind tunnel and leading the pressure tubes to the pressure transducer. The right wing is a basic wing with holes

for mounting. These two parts can be seen in figures 5.3a and 5.3b. Aligning the three wing sections has to be fairly accurate. The center wing thus carries threaded holes, and the adjacent wings have M4 holes where a threaded rod can align the wings securely. The final design of the centrepiece can be seen in figure 5.2.

Material selection is based on the ease of machinability - a CNC-miller was provided to us, along with ample amounts of aluminium. This scale wing is not to be used in the actual race car, so weight is not a concern. Construction of the 1/4 scale wing is not trivial. High precision is required for the surface finish, and the pressure taps have to be small in diameter:  $\phi 0.8$  mm and very deep. This is not an ordinary task and requires specialized tooling.

The manufactured model wing can be seen in 5.4, taken shortly after receiving the parts back from Rasmus Himborg. The width of the centrepiece is based around the fact that potential upstream interference from misalignment of the wing profile sections would not cause issues around the pressure taps.

### 3D-printed parts

Due to machining cost and production time, the second element was 3D-printed on A Zortrax M200 3D printer at DTU Skylab. The two 3d printed parts were glued together using instant glue.

### Assembly

In figure 5.5 the down-scaled wing post-production with pressure tubes inserted can be seen with pressure-taps along the centrepiece. The wing is assembled by laser cutting the two end plates with holes for mounting, as well as the H7 mounting hole and exits for the pressure tubes.

In order to strengthen the construction and smoothen the surface, the 3D-printed rearwing was reinforced using red tape (as seen in figure 5.5), and is additionally supported by a wooden centrepiece holding the two wings together. Lastly, the small wing is reinforced further by attaching screws through the end plate, ensuring the wing does not rotate.

### 5.3. Experimental Procedure

---

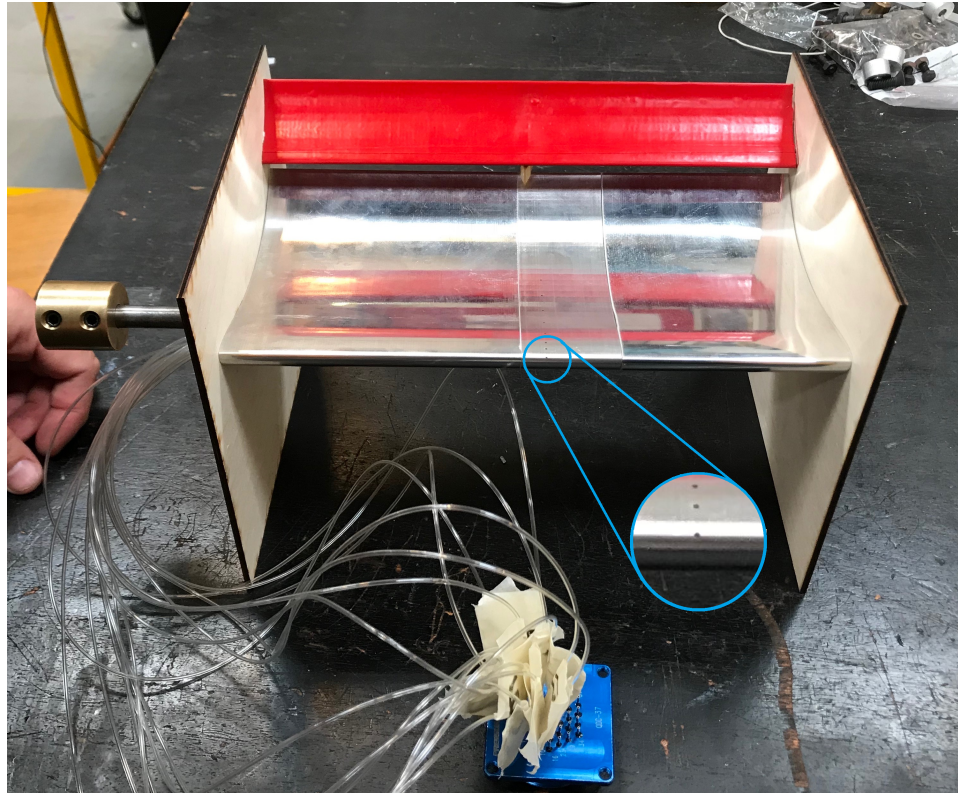


Figure 5.5: Down-scaled wing assembled with a zoom in on the pressure taps. The length of the entire wing is approximately 250 mm with a total chord length of 150 mm.

## 5.3 Experimental Procedure

The model wing's  $\varnothing 8\text{ mm}$  hole is fitted with a rod at the end as seen to the left in figure 5.5, which is then mounted to the force gauge at the bottom of the wind tunnel. It is important the wing is placed as close to true level, in order to not get a skewed angle of attack initially [18]. The pressure measurement tubes are passed through a hole in the bottom of the wind tunnel's test section. Connection is established to the LabVIEW software running on a nearby computer. A picture of the data collection UI can be found in appendix A.1.

The wing is positioned with a  $0^\circ$  angle of attack. Measurements are taken with  $10\text{ m s}^{-1}$  increments in the range of  $10\text{ m s}^{-1}$  to  $60\text{ m s}^{-1}$ , with an angular sweep at  $20\text{ m s}^{-1}$  and  $40\text{ m s}^{-1}$  to compare the optimum angle of attack with literature.

However, due to the wing covering a relatively large area of the wind tunnel, the final test could only go to  $59.2\text{ m s}^{-1}$ , which corresponds to

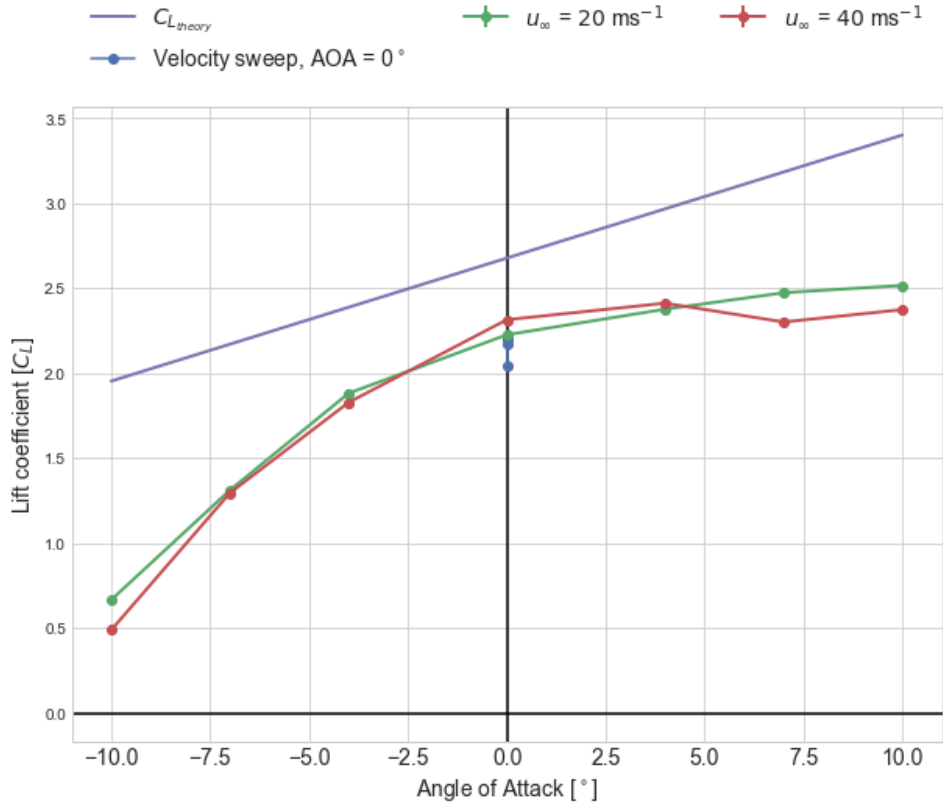


Figure 5.6: The lift coefficient plotted as a function of the wing's overall AOA. The wing's own angle of attack is  $35^\circ$ , which is beyond the theoretical optimum as seen in figure 4.1.

$14.8 \text{ m s}^{-1}$  or  $53.3 \text{ km h}^{-1}$ . Albeit slightly lower than optimal, it is not far out of the proposed range.

## 5.4 Results

The results from the experiment is divided into two parts: A comparison with the theoretical lift values of the downscaled wing, and a comparison with the simulated results. The simulated results will be shown in section 6.3, while the comparison to theory can is shown below.

The theoretical lift coefficient at of the scale wing using a total AOA of  $\alpha = 37^\circ$ , an effective additional AOA from the wing's camber of

## 5.4. Results

---

$\alpha_{L_0} = 0^\circ$  and equation 3.5 is found to be:

$$\begin{aligned} C_L &= \left( \frac{2\pi}{1 + \frac{2}{\frac{b}{c}(1+1.9\frac{h}{b})}} \right) (\alpha + \alpha_{L_0}) \\ &\Rightarrow \left( \frac{2\pi}{1 + \frac{2}{\frac{250\text{mm}}{150\text{mm}}(1+1.9\frac{175\text{mm}}{250\text{mm}})}} \right) \left( \frac{37\pi}{180} \right) = 2.68 \end{aligned}$$

Comparing the theoretical lift to the lift coefficients found by the experiments is seen in figure 5.6. The purple line is the theoretical lift, where the wing's angle is swept between  $-10^\circ$  and  $10^\circ$ . The measured lift is slightly lower than the theoretical, which may be explained by the end plate's effect on aspect ratio. The downscaled wing has a very large  $\mathcal{R}$ , where the end plates extend far below the bottom of the wing. While theoretically beneficial, the effect of the long end plates might not extend all the way up to the wing profile, artificially inflating up the theoretical lift number. Another effect is seen in figure 5.7, albeit a bit difficult to see, the end plates bend down due to the lower pressure between the endplates. This might have reduced flow underneath the wing, constricting airflow and reducing the overall lift. The deflection was approximately 10 mm on each end plate.



Figure 5.7: The upper end plate can be seen deflecting slightly downward due to the lower pressure between the endplates.



# 6

## Simulation

The simulation will run in several parts. First, the wings relative placement between each other will be optimized in a 2-dimensional environment. This involves,  $x$ - and  $y$ -distance between the multi-element wings, angle of attack and height relative to the chassis to give a good estimate of the wings placement range. Secondly, a 3-dimensional analysis of the entire wing with endplates will be performed to compare with results from the wind tunnel test.

### 6.1 Star-CCM+

Star-CCM+ was used to run the simulations of the wing first in the windtunnel for verification. As meshing and running the simulations were heavy computational tasks, the computations were run on the Niflheim Linux cluster supercomputer, which is installed at the Department of Physics at DTU.

The program numerically solves the Navier-Stokes equations, which are derived by the conservation of energy, mass and momentum through a volumetric flow. As Star-CCM+ uses the finite volume method, the equations are discretized to the conservative form: The in- and outgoing flux through a control volume must be conserved. Mathematically, this is expressed as:

$$\frac{\delta}{\delta t} \iiint Q dV + \iint F dA = 0 \quad (6.1)$$

## 6.2. Mesh Generation

---

Where  $\mathbf{Q}$  is the vector of the conserved variables (eg.  $\rho$  = density),  $\mathbf{F}$  is the vector of fluxes(eg.  $\rho\mathbf{u}$  = mass flux,  $\rho\mathbf{u}^2 + p$  = momentum flux + pressure force) and  $V$  is the control volume element and  $A$ is the surface area of the control volume element. The turbulence model Star-CCM+ employs is a K-epsilon turbulence model which is the most commonly used in computational fluid dynamics.

The reader interested in how Star-CCM+ works is referred to the User Guide Star-CCM+, version 13.02.

## 6.2 Mesh Generation

<<< HEAD The mesh has to be structured in accordance to best practice. Areas with high velocity and pressure gradients have to be dissolved in acceptable resolutions, in order to ensure correct results. Running an initial test on a generic mesh made it clear where the volume mesh requires greater resolution. Gradients are easily visible around the wing's leading edge, and generally around the solid bodies. Furthermore, aligning the mesh with the flow improves accuracy and rate of convergence. To determine the convergence of simulation results six different mesh resolutions where used to examine the simulations for the windtunnel setup with a wind velocity of  $40 \text{ m s}^{-1}$ . Finding the minimum mesh resolution where results have converged with higer resolution results, means a minimum computation time can be achieved and thereby allowing for more simulations to be run. ====== The mesh has to be structured in accordance to best practice. Areas with high velocity and pressure gradients have to be dissolved in acceptable resolutions, in order to ensure correct results. Running an initial test on a generic mesh made it clear where the volume mesh requires greater resolution. Gradients are easily visible around the wing's leading edge, and generally around the solid bodies. Furthermore, aligning the mesh with the flow improves accuracy and rate of convergence. To determine the convergence of simulation results, six different mesh resolutions where used to examine the simulations for the wind tunnel setup with a wind velocity of  $40 \text{ m s}^{-1}$ . Finding the minimum mesh resolution where results have converged with higer resolution results, means a minimum computation time can be achieved and thereby allowing for more simulations to be run. >>> a678bbb7eb35b75ff4105b50183073fe790d8144

Generating a mesh of correct size is done by sampling downforce over

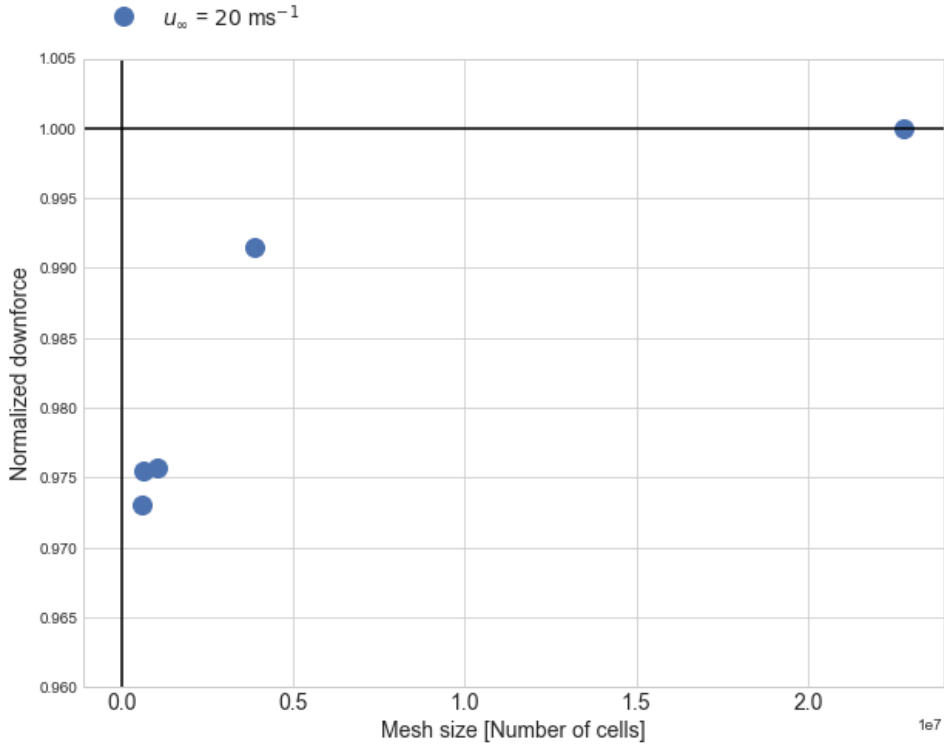


Figure 6.1: Normalized downforce as a function of mesh size. Plotted to see the convergence towards the same force.

a range of mesh sizes. In figure 6.1, the normalized downforce is plotted as a function of the mesh size. The mesh independence study shows that the function converges to acceptable levels near the mesh size  $0.4 \times 10^7$ , and serves as a good compromise between results and computing time.

### 6.3 Verification of Simulation Results

The data from the experimental test with the  $\frac{1}{4}$  scale model was first plotted to obtain an idea of the surface pressure distribution on the test wing. An example of a mean over 3000 pressure readouts for a wind speed of  $40 \text{ m s}^{-1}$  is shown in figure 6.2, with the standard deviation shown as errorbars. Measurements were run in wind tunnel from  $10 \text{ m s}^{-1}$  to  $60 \text{ m s}^{-1}$  in steps of  $10 \text{ m s}^{-1}$ .

Simulations were then run in Star-CCM+. Firstly the CAD model of the  $\frac{1}{4}$ -scaled wing was imported into the software, then the dimensions of the red wind tunnel was drawn and the CAD model was placed

### 6.3. Verification of Simulation Results

---

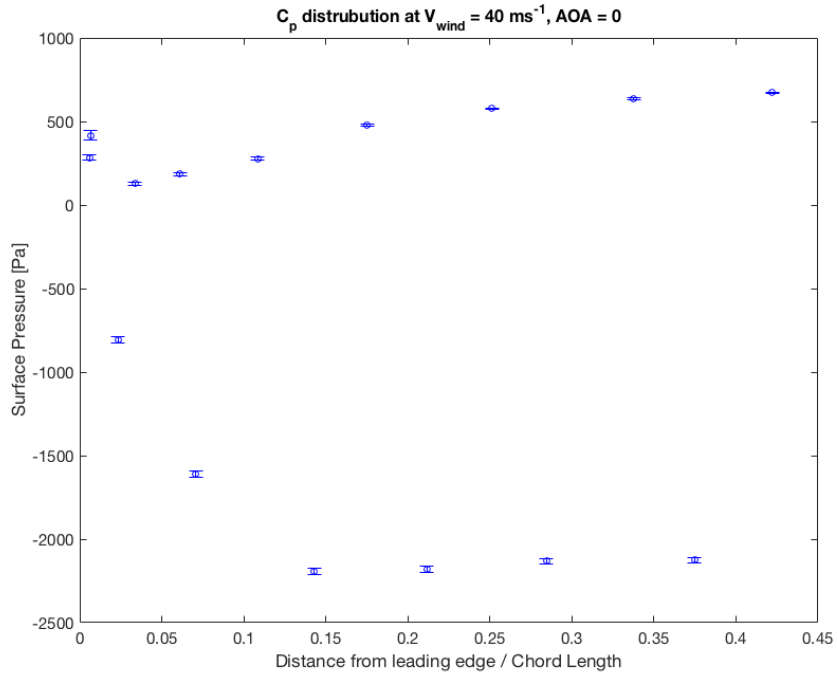


Figure 6.2: Surface pressure readout from the 15 pressure taps located on the model at wind speed  $40 \text{ m s}^{-1}$  in the wind tunnel. Pressure readout is meaned over 3000 measurements and shown with errorbars representing the standard deviation of the measurements.

in the same location as in the real test. The setup was then volume meshed with a cell count of around  $0.4 \cdot 10^7$  cells as found in section 6.2 to be adequate for convergence of results. A 2D view of the volume mesh is shown in figure 6.3. After meshing, the physics model for the simulation is setup, and simulations are run for the different wind velocities.

The 3-dimensional simulations were run until the simulation results converges. Monitors of the dragforce and downforce for the wing found by the simulation were used to determine the convergence of the results, an example of the convergence plot is shown in figure 6.4. Furthermore scalar views and vector views of the pressure distribution and wind velocity around the wing profile can visually help verify that the solutions does not have any obvious faults, such as areas with extremely high velocity og pressure indicating the found solutions are not realistic. Examples of a scalar view for the pressure distribution and a vector view of the wind velocity are shown in 6.5 and 6.6.

From the simulations the surface pressure of the airfoils was also found,

### 6.3. Verification of Simulation Results

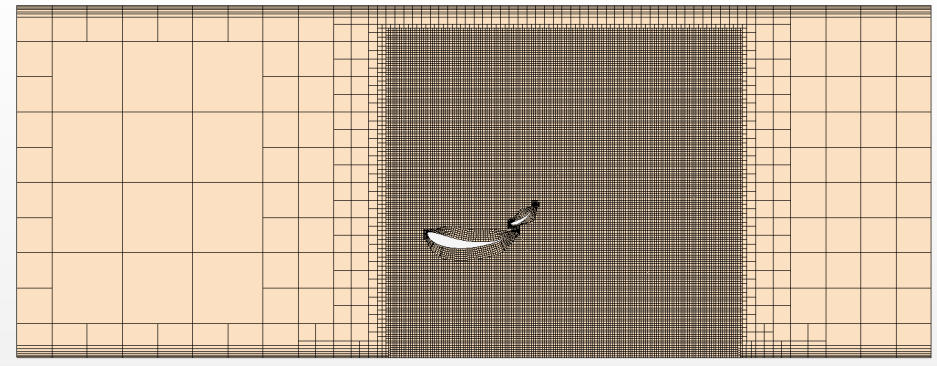


Figure 6.3: 2D cut through of the volume mesh used for simulations of the wind tunnel test. Mesh size is approximately  $0.4 \cdot 10^7$  cells.

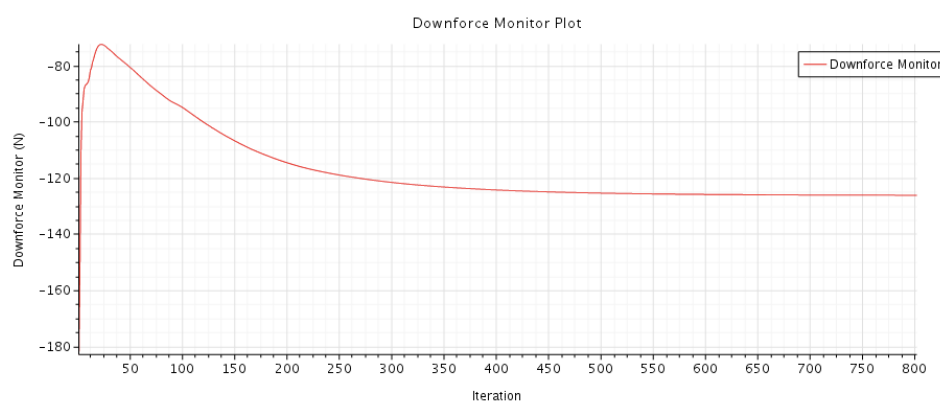


Figure 6.4: Monitor of the convergence of the downforce over the number of iterations in Star-CCM+, here shown for a wind velocity of  $40 \text{ m s}^{-1}$ .

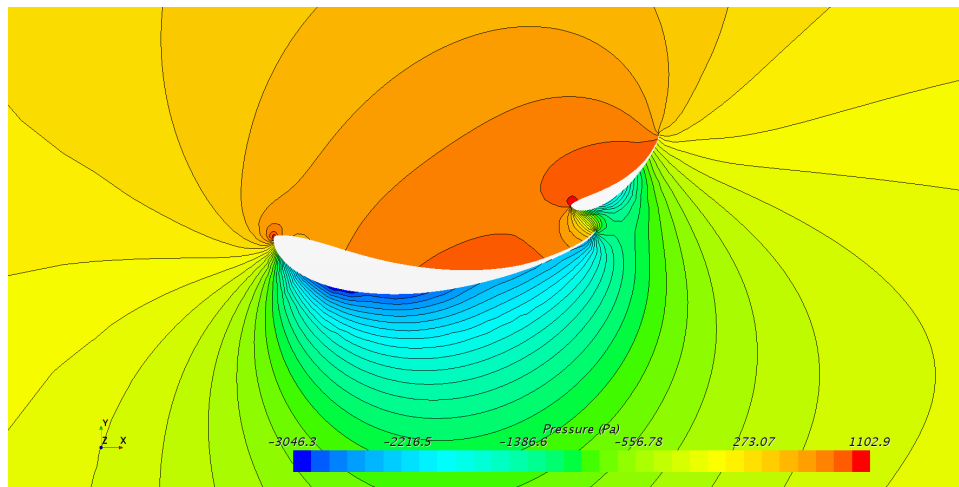


Figure 6.5: Scalar view of the pressure distribution surrounding the two elements of the wing, here at a wind velocity of  $40 \text{ m s}^{-1}$ .

### 6.3. Verification of Simulation Results

---

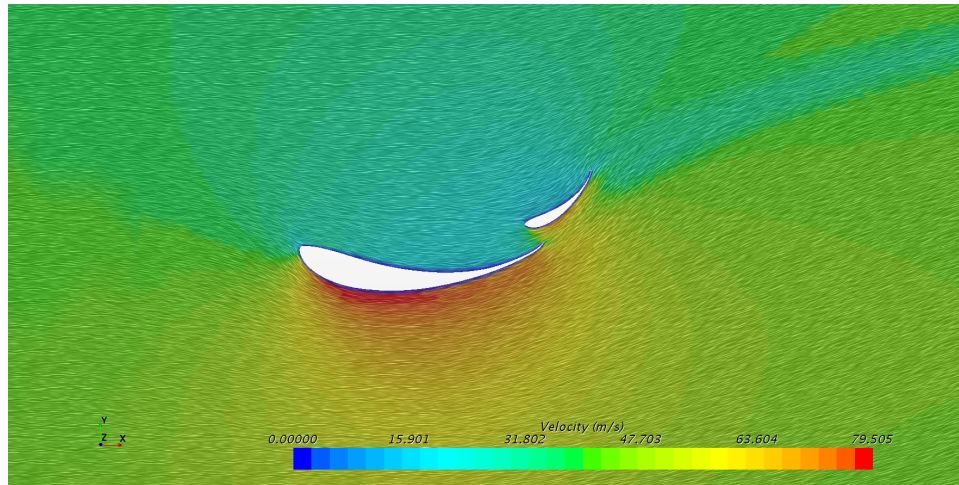


Figure 6.6: Vector view of the wind velocity surrounding the wing, here at a wind velocity of  $40 \text{ m s}^{-1}$ .

and saved to compare with the measurements of the surface pressure from the real wind tunnel test. The simulated surface pressure is shown in figure 6.7.

Comparing the surface pressure predicted by the simulation, figure 6.7, and measured in the test, figure 6.2, show that the pressure values are not close. Furthermore comparing the by simulation predicted downforce and measured in the test downforce, shows that the simulated results predict a 40 % higher amount of downforce than measured. This could be caused by several factors. One factor could be the assembly of the test wing is not a perfect replica of the full scale wing, an improvement to help this would be by producing the scaled model completely by machining with small tolerances, compared to the half machined and half hand-build model used in these test. This could cause the relative position of the two wing elements to be different from the CAD model used in simulations.

Finding the correct correlation between the estimated downforce and exact surface pressure will not be possible in this report. The simulations and measurements can however be compared by using the dimensionless number, the pressure coefficient,

$$C_p \equiv \frac{p - p_\infty}{\frac{1}{2} \rho_\infty V_\infty^2}, \quad (6.2)$$

where  $p$  is the static pressure at the point being evaluated,  $p_\infty$  is the

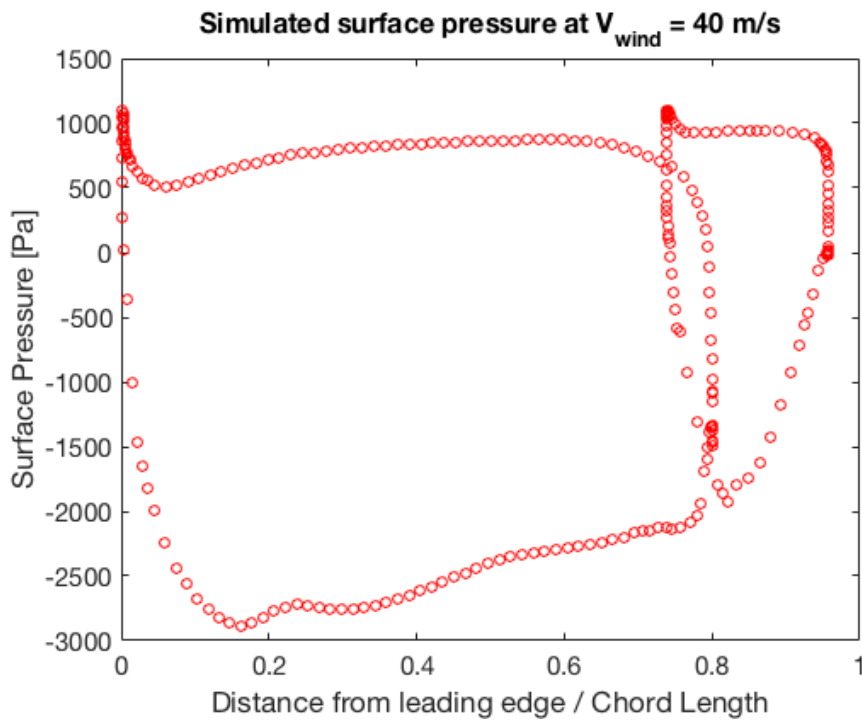


Figure 6.7: Simulated surface pressure on both elements of the wing. To the left: the larger elements surface pressure and to the right the smaller elements surface pressure is shown. Simulated at wind velocity of  $40 \text{ m s}^{-1}$ .

static pressure in the freestream,  $\rho_\infty$  is the freestream fluid density and  $V_\infty$  is the freestream velocity of the fluid. The pressure coefficient describes the relative pressure throughout a fluid in movement. The highest possible for  $C_p$  is 1, which occurs at the stagnation point, where the fluid comes to a complete stop. In many situations the pressure coefficient near a body is independent of the size of the body.

**Fixme Fatal:** Consider moving to theory

The pressure coefficient therefore allows us to compare the form of the relative pressure between the simulations and the experimental test. This comparison is shown in figure 6.8. When comparing the two, a difference in value is still visible due to the difference in absolute pressure, but the form of the two  $C_p$  distributions, confirm the characteristics of the flow around the wing is obtained through the simulation. A higher resolution of measuring taps would help further testing, but for the smaller model is very difficult to achieve due to lack of space.

**Fixme Fatal:** fix labels. fixed

The use of simulations for designing an aerodynamic package for the race car for the moment is useful as a way to insure the relative pressure distribution around the wing is as wanted, and ensuring that the flow

### 6.3. Verification of Simulation Results

---

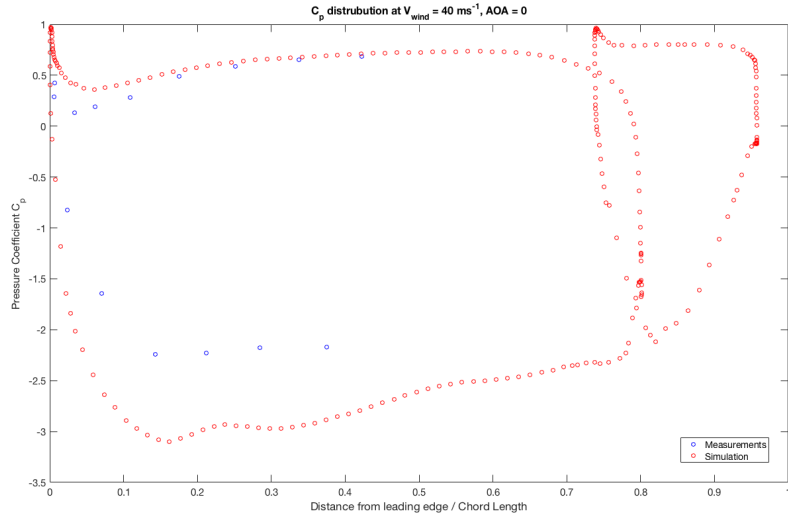


Figure 6.8: Comparison of simulated and test found  $C_p$  values at a wind velocity of  $40 \text{ m s}^{-1}$ .

does not separate at unwanted locations. However further work on the correlation between simulated downforce and measured downforce is still needed and the work will continue with the Vermilion Racing team, in order to have the best possibilities to design a good aero-package before having to build it.

Lastly worth noting is when the simulated flow is visualized by streamlines, the vortex generation at the rear of the wing, as mentioned in section 3.1.3, is shown clearly in figure 6.9. It is clear that the size of the produced vortices are interacting with the side walls of the wind tunnel. A suggestion for further testing of an wing with such large vortex generation would be to use a wind tunnel with a larger cross-section to avoid interactions with the side walls.

#### 6.3.1 Multi-Element Wing Optimization

The influence of the two wing elements relative position on lift was examined to optimize the downforce further. This relative position optimization was performed in the software package MultiElements Airfoils provided from Hanley Innovations. A scatterplot of the relative position is seen in figure 6.10. The trailing edge of the first element is seen as the dark outlines, and the position of the second element's leading edge is plotted, where the resulting lift coefficient is embedded as color. The redder the better lift coefficient. After sweeping, a

### 6.3. Verification of Simulation Results

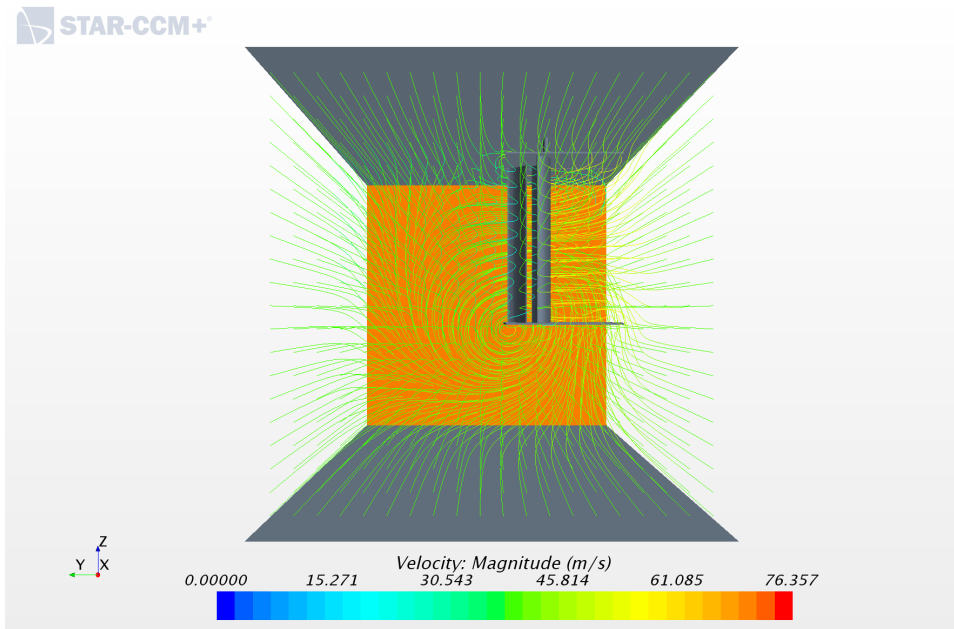


Figure 6.9: Visualization by streamlines of the simulated airflow around the wing. Vortex generation at the rear of the wing is visible.

maximum lift of  $C_L = 2.60$  at  $u = 15 \text{ m s}^{-1}$ . is found with the leading edge of the secondary element placed at  $x = 0.5 \text{ m}, y = 0.01 \text{ m}$  relative to the leading edge of the main element.

### 6.3. Verification of Simulation Results

---

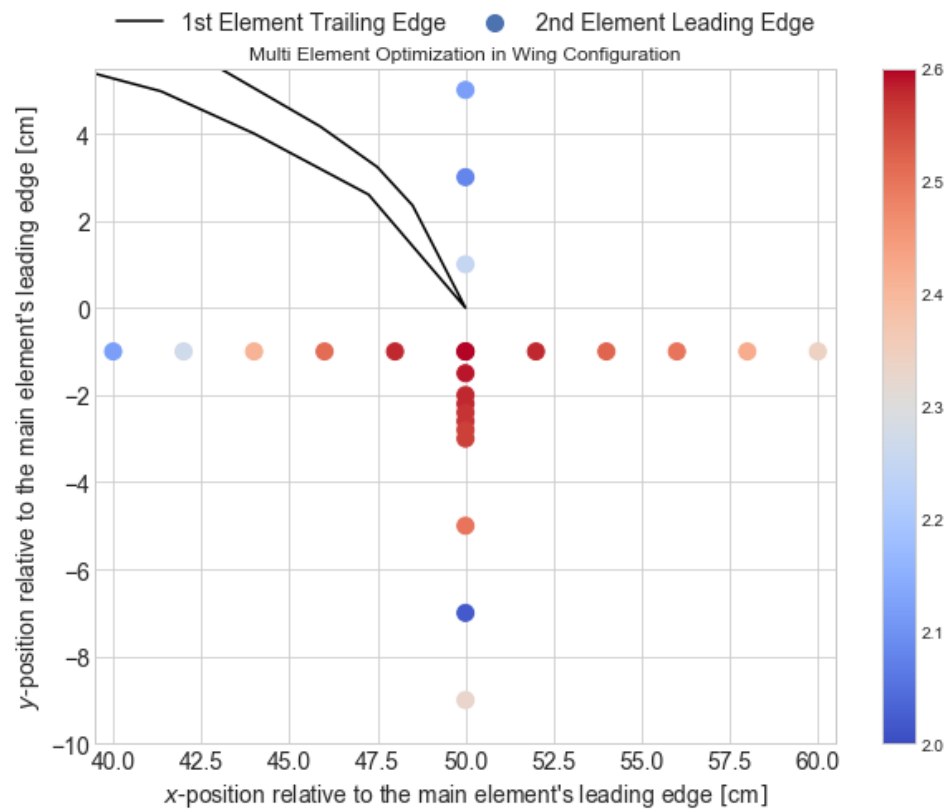


Figure 6.10: Optimization of the two element wing. The redder the dots, the higher the lift coefficient.

# 7

## Construction

This chapter concerns the construction of the rear wing. The step from theoretical abstraction to a real product. This includes dimensioning, material selection and finalizing the wing. The simulated rear wing lacks a proper mounting method, as the design depends on the external group at Vermilion Racing.

### 7.1 Requirements

The formula student competition has a clear ruleset dictating the strength requirements of aerodynamic devices. The most crucial elements are outlined below:

#### 7.1.1 Strength Requirements

The competition rules set up strength requirements for the aerodynamic devices, making sure wobbling or unsafe structures are prohibited. The rules are seen below:

### 7.3. Composites

---

Aerodynamic Devices Stability and Strength:

- T7.5.1 Any aerodynamic device must be able to withstand a force of 200 N distributed over a minimum surface of  $225 \text{ cm}^2$  and not deflect more than 10 mm in the load carrying direction.
- T7.5.2 Any aerodynamic device must be able to withstand a force of 50 N applied in any direction at any point and not deflect more than 25 mm.

Rules from Formula Student UK 2018 ruleset [4].

Thus, deflection of the wing has to be calculated, in order to comply with the rules.

## 7.2 Material Selection

Selecting a fitting material depends on the maximum deformation and weight. According to the PDS (see section 4.3), the wing has to be as light as possible in order not to move the center of mass further upwards. Furthermore, it needs a high elastic modulus in order to be stiff as to not deform by aerodynamic forces. The wing needs to be have a high yield strength, be low cost and easy to produce time wise.

Drawing on experience from competitors, carbon fiber- and glass fiber reinforced polymers are the weapons of choice [19]. However, Cambridge Engineering Selector, a material selection tool was used in order not to leave a stone unturned. The results can be seen in figure 7.1, where materials of high elastic modulus are plotted against their density. Magnesium and some aluminium alloys are near the carbon fiber reinforced polymers, but machining an entire wing out of metal is incredibly time consuming and expensive. Carbon fiber reinforced polymers are chosen as a material, and the next chapter will investigate the properties and strength of the composite structure.

## 7.3 Composites

The geometrical shape of a composite structure can be highly varied, which can increase strength dramatically. The second moment of inertia of a simple beam can be increased by moving material from the neutral axis, as is done in a standard I-beam. The same thing applies

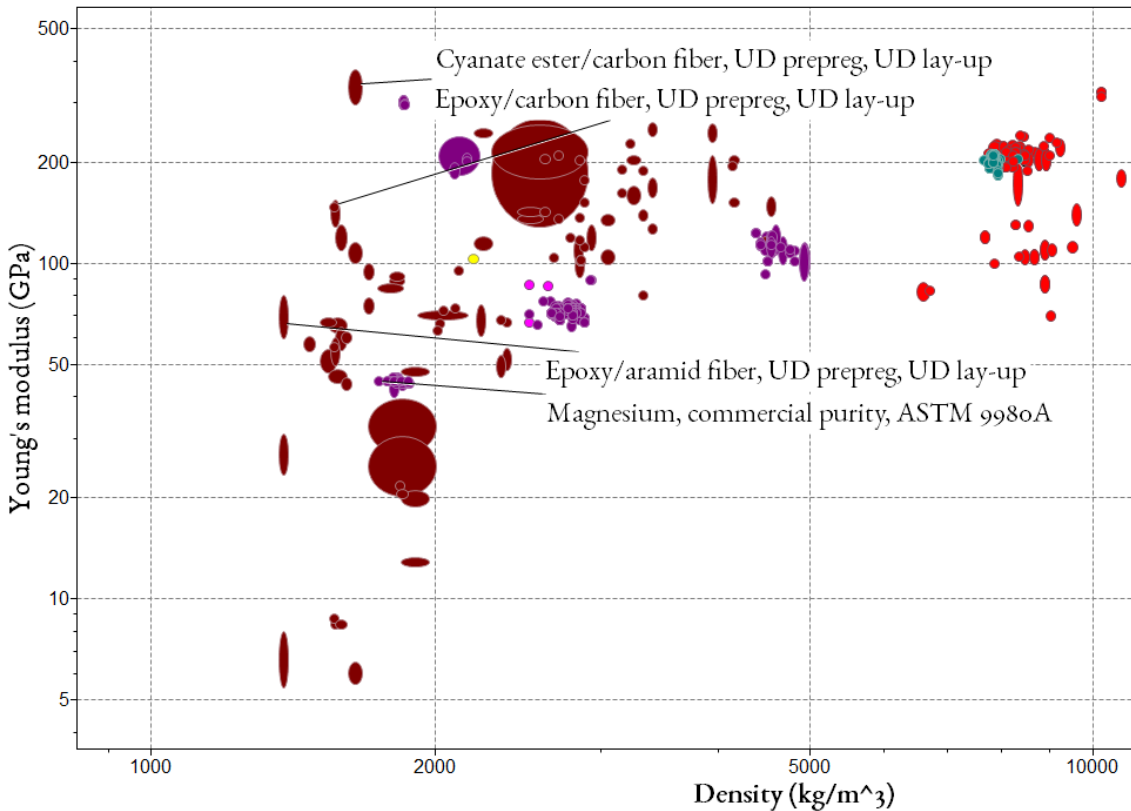


Figure 7.1: Cambridge Engineering Selector (CES) showing the various aerospace grade materials usable for this application. The dark red dots are composites, while the dark purple dots are metals such as aluminium and magnesium.

to composites: A soft, but light core can be added with a hard shell (in this case carbon fiber) surrounding the core.

An approximation of the wing profile is a box shape, where the moment of inertia is much easier calculated. From [20], the strength of the sandwich material can be mathematically described as:

$$D = EI = E_{cs} \frac{bh^3 - ec^3}{12} + E_c \frac{ec^3}{12} \quad (7.1)$$

Where  $E_{cs}$  is the elastic modulus of the composite shell,  $E_c$  is the elastic modulus of the core,  $b$  is the width of the beam,  $h$  is the height of the beam,  $e$  is the width of the core and  $c$  is the height of the core. The strength of a fiber composite depends on the fiber direction, the relationship between the fiber and matrix, and the porosity of the composite. The load bearing properties in the fiber direction is given

## 7.4. Final Design of Rear Wing

---

by:

$$E_{\text{long}} = E_f \text{Vol}_f\% + E_m(1 - \text{Vol}_f\%) \quad (7.2)$$

Where  $E_f$  is the elastic module of the fiber and  $E_m$  is the elastic modulus of the matrix. The  $\text{Vol}_f\%$  is the fiber volume fraction of the composite. For a transverse load, which is what rule T7.5.1 and T7.5.2, the strength of the sandwich construction is found as:

$$\frac{1}{E_{\text{transverse}}} = \frac{\text{Vol}_f\%}{E_f} + \left(1 - \frac{\text{Vol}_f\%}{E_m}\right) \quad (7.3)$$

For the biaxial carbon fiber weave used in this construction, the strength is almost 50% less in the transverse direction [20]. The effective elastic modulus is found to be  $\approx 60$  GPa. Using the beam approximation that the deflection of the rear wing functions as a beam with a core supported in both ends is found to be: [21]

$$\delta_{\max} = \frac{PL^3}{192EI} = 0.03 \text{ mm} \quad (7.4)$$

Which is far below the maximum allowed by a factor of more than 300. This also ensures the wing keeps its dimensions even though a high downforce is present.

## 7.4 Final Design of Rear Wing

Designing the final design can be done based on the investigations produced in the previous chapters. First, the FSUK rules restrict the cross sectional dimensions, as seen in figure 4.2. Thereto, the rule T7.3.2 All aerodynamic devices higher than 500 mm from the ground, must not extend outboard of the most inboard point of the rear wheel/tire dictates the width of the wing. According to the car's current design, the inner dimension from wheel to wheel is 1100 mm, and thus serves as the maximum width of the wing.

The two elements of the full scale wing will be bolted to the endplates at the optimal found angle of attack. The wing elements will have two metal brackets glued to the inside of the carbon fiber wings, the bracket will have holes with M10 threads in which the endplates are bolted to secure the structure. The structure can be seen in figure 7.2, with end plates, brackets, wings and bolts.



Figure 7.2: Render of the final design of the rear wing in exploded view.

#### 7.4.1 Topology Optimization of Wing Brackets

In order to minimise the weight of the metal bracket inserts topology optimizations were made using the build in function in Fusion 360, in which all simulations are done in the cloud. Topology optimization tries to reduce the weight of the model by removing excess material while maintaining stiffness and strength of the model.

The inserts were modelled from the wing profile and the location of the inner threads was chosen. The model was then meshed with a target cell size of 1.5 mm, and the target weight reduction was set to 70%, with a downforce load of 250 N at the surface.

The result of the optimization for the large insert is shown in figure 7.3, was then used to remove excess material from the model. The results were overlaid on the model and material could be cut from the original model as shown in figure 7.4. The final model of the large insert was then created with a weight reduction around 40 %. A render of the final model is shown in figure 7.5. The same procedure was done for the smaller metal wing insert, and technical drawings of are included in following section.

The two elements of the full scale wing will be bolted to the end plates at optimal found angle of attack. The wing elements will have two

Fixme Note: Not there.  
Where should they be?

## 7.4. Final Design of Rear Wing

---

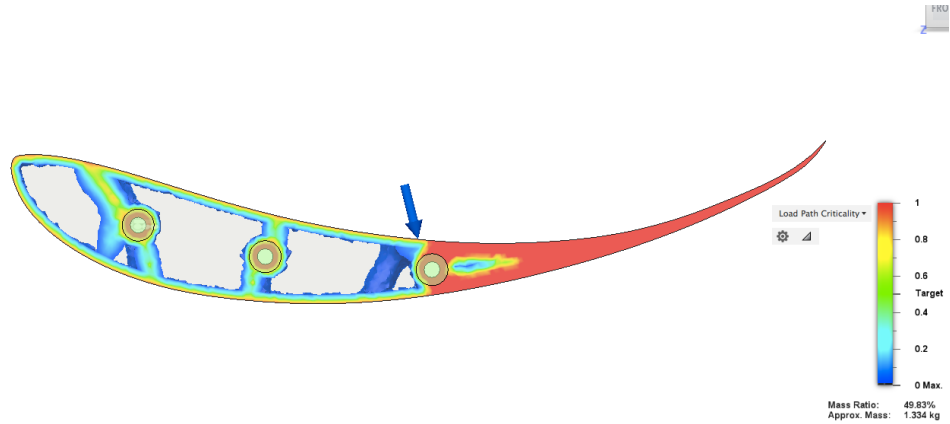


Figure 7.3: The result of the topology optimization for the large insert, with a weight reduction at about 50 %.

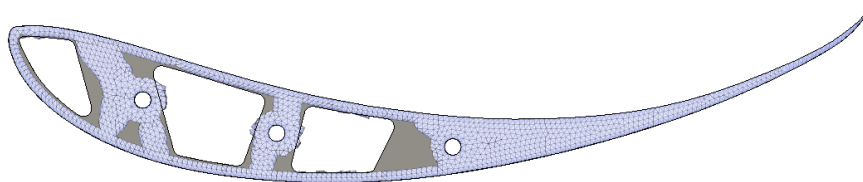


Figure 7.4: Optimized mesh overlayed on model so excess material could be easily removed.



Figure 7.5: Render of the final model for the metal insert, with a weight reduction around 40 %.

metal brackets glued to the inside of the carbon fiber, the bracket will be have holes with M10 threads in which the endplates are bolted to secure the structure.

## 7.5 Manufacturing Final Design

The following section describes the steps required to build the wing physically. First, templates of the MSHD airfoil are lasercut. The templates are mounted on the sides of polystyrene blocks, where a homemade hot wire cutter cuts the foam cores of the wing. The foam cores are then glued together into the appropriate lengths, where the carbon fiber mattes are draped over. The carbon fiber is then reinforced by an epoxy resin, which over a 24 hour period is hardened. The surface is then polished, and finally resealed by adding another layer of epoxy resin. The wing is then bolted to the end plates through the two metal brackets inserted into the wing's ends.

### 7.5.1 Polystyrene Moulds

The moulds for the wings were chosen as positive moulds, meaning polystyrene moulds of the actual wings were cut out and overlaid with resin coated carbon fiber. In order to do this, we devised a hot wire-based specialized tool for the job. This can be seen in figure 7.6, where a 0.3 mm heat resistant wire was used at 12V drawing 2.5 A over a cutting length of 600 mm. In order to get the correct airfoil shapes, the MS HD airfoil profile was lasercut out of 3mm plywood. The wooden profile is then mounted on the sides of the polystyrene block, where the hotwire is pulled across in a timely fashion. In order to produce a smooth surface, two people have to move very coordinated. Going too slow leaves deep melting lines, and moving too fast makes the hotwire "slack" in the middle as it does not have enough energy to melt the polystyrene quick enough, causing the airfoil profile to be skewed.

All hotwire cutting was done by hand over several days, and we owe a special thanks to our sponsor DTU Skylab for providing the polystyrene blocks.

## 7.5. Manufacturing Final Design

---



Figure 7.6: The hot wire melts the styrofoam while sliding along the wooden template.



Figure 7.7: Steffan and Nicolai performing a hand layup of the carbon fiber mats around a polystyrene foam core.

### 7.5.2 Hand Layup

The finished positive moulds are used both as moulds where carbon fiber is applied on, as well as foam cores that reinforce the structure. The moulds are then placed inside the negative forms of the moulds, where carbon fiber is draped over the surface. The epoxy is then applied to the carbon fiber matte by a soft brush, and air is rolled out by spiked rollers. Nicolai Boertman is seen performing this action in figure 7.7, putting the final layer on the main element of the rear wing. The white polystyrene mold underneath the carbon fiber is the negative mold, which helps keep the shape when applying to carbon fiber to the other side. After rolling out the epoxy satisfactorily, a plastic tarp is added to the surface and rolled down neatly without air bubbles. This ensures getting a smooth surface, and lets the wing cure in a closed environment.

Three methods of curing was attempted:

The wing hanging freely with no pressure: The results was good. No pooling of epoxy, the surface was relatively smooth, but an additional sealing layer had to be applied, as the epoxy had been displaced from the surface. This gave it the surface roughness of the fibers, which is

## 7.5. Manufacturing Final Design

---



Figure 7.8: Curing the wing in a flat position lets the resin pool in the center of the wing. This causes the surface to be very rough, potentially causing the boundary layer to trip early. A very unwanted effect that requires mending.

not optimal.

The wing laying flat under pressure with the convex shape pointing upwards: This was highly successful, giving a very smooth surface with the right amount of epoxy covering it. No additional treatment was required.

The concave shape pointing upwards: The results was not good, but workable. The results can be seen in figure 7.8. The epoxy pooled due to gravity forcing the epoxy down towards the center of the cambered wing. Getting a proper surface finish from this is handled in the section below.

### 7.5.3 Surface Finish

Curing should occur by securing the wing vertically or with the convex shape pointing upwards, as to not let epoxy pool up on the concave surfaces. This knowledge was forgotten on one of the wings, as seen



Figure 7.9: Sanding the wing clears the surface roughness, but requires a new layer of sealant. Using epoxy or a lacquer was investigated before settling on epoxy.

in figure 7.8, where the surface has become very rough due to epoxy pooling. Albeit not optimal, the wing can be salvaged by sanding. The finished product after sanding and preparing the surface is shown in figure 7.9. The surface finish is done with a thin layer of extra epoxy. Using a clear lacquer was also investigated, but the reduced durability of the lacquer is not optimal [22]. The wing has to survive transport to England, which can damage a soft surface.

## 7.6 Final Assembly

The final assembly of the wing is going to be done in July before competition start. A complete design of the wing is not feasible at this stage, due to many unforeseen changes in how the rear of the car is going to fit together. The wing is not essential for a bare minimum product, which is why the fitting hereof is not a priority for the team as a whole.



# 8

## Discussion

The following section will discuss the results in chapter 5, the simulations made in chapter 6 and the design in chapter 7. The purpose of this paper was to investigate the effects of aerodynamics on race cars, design a solution that would improve the car's lap time and begin manufacturing the hypothesized aerodynamic device.

### 8.1 Theory, Experiments and Simulations

The wind tunnel results plotted in figure 5.6 shows a correlation between the wing's lift and theoretical lift, assuming a constant  $C_L$  for the theoretical wing. The experimental results are all lower than the theoretical, which may be due to several facts: First, the wing section's was misaligned due to the forces operating at higher speeds as one section twisted, creating a small gap of 2 mm to 3 mm between the wing sections. Secondly, the wing's extremely high lift interferes with the flow behaviour, as the wing's wake is most likely pushing air against the walls. This theory is corroborated by the simulations as seen in figure 6.9, where it is clearly seen that the wake vortex interferes with the wall's boundary layer. Third, and most likely the most important, the placement relative to each other may be slightly off. Creating a small multi element airfoil is very difficult, as placement is everything to the lift of the wing. According to the wing optimization process seen in figure 6.10, very small changes can rapidly change the lifting characteristics of the wing. This could explain why the lift of the air-

### 8.3. Factual Improvements

---

foil model is much lower than the theoretical, and the fact that the simulations coincide very well with theory.

After evaluating the experimental results and the simulations, it was clear that an investigation of the down scaled wing model was due. This revealing a relative position of the trailing-edge-to-tip position of  $(x, y) = (11.5 \text{ mm}, 8 \text{ mm})$ , instead of the planned  $(6.9 \text{ mm}, 12.5 \text{ mm})$ . The variation comes from placing the wing initially, which fits the theory mentioned in the above section. The importance of the position was not uncovered until simulations optimizing their relative position, and due to time the experiment was not redone. However, a simulation using the new relative position of the wing was performed, showing a change in lift from  $C_L = 2.50 \rightarrow 2.43$  due to misplacing the second element. Additionally, the angle of the second element is of great importance to the lift, removing in the excess of 20% of the lift coefficient if wrongly placed. The lesson learned is that the second element must be very carefully placed relative to the first element, in order to not alter the flow substantially.

This can be directly transferred to the construction of the full scale wing, making it a valuable lesson to learn in the wind tunnel.

## 8.2 Product Design Specification Review

The finished product have to live up to the design specification, in order to be a useful solution. In table 8.1, it can be seen that all requirements are fulfilled, and all criteria except one. During the design process of the car, the removal of the engine became negligible as the battery pack is going to be removed in another way. This voids the criteria, and thus makes the solution an optimal one.

### 8.3 Factual Improvements

The theoretical lift coefficient found from simulations is shown to be  $C_L = -2.8$ . For a complete lap time simulation the entire aerodynamics package has to be finished. Numbers from the initial calculations of the front wing and undertray provide an estimated total lift coefficient of the car to be around  $C_L = -2.4$  [5]. As seen in figure 8.1, this should increase the tight cornering speed from with 4 – 5%, while for larger radius corners upwards 20 – 35%!

### 8.3. Factual Improvements

Issue	Requirement	Criteria
Weight	Must not move CM above halfway point	Should be as low as possible
Safety	Must be in compliance with FSAE rules	Should not make handling difficult for driver
Durability	Must have no fatigue limit. Must be waterproof	
Performance	Must have high down-force & soft stall characteristic at all speeds	Should retain performance despite tripping. Should have end plates.
Dimensioning	Must be within area defined by FSAE rules	Should allow space for motor removal.
Production	Must have low time- and monetary cost	

Table 8.1: The PDS table shows how the final design lives up to the proposed specifications.

While fulfilling the PDS, the ease of production and being a first design ever restricted the scope of the project. Great improvements can be expected in the coming years. The extend of the theory required in order to produce a rear wing has been uncovered, and this project serves as a guideline for future iterations of the rear wing. In chapter 9, a series of possible improvements are evaluated and proposed for increasing the aerodynamic contribution to increasing lap times.

### 8.3. Factual Improvements

---

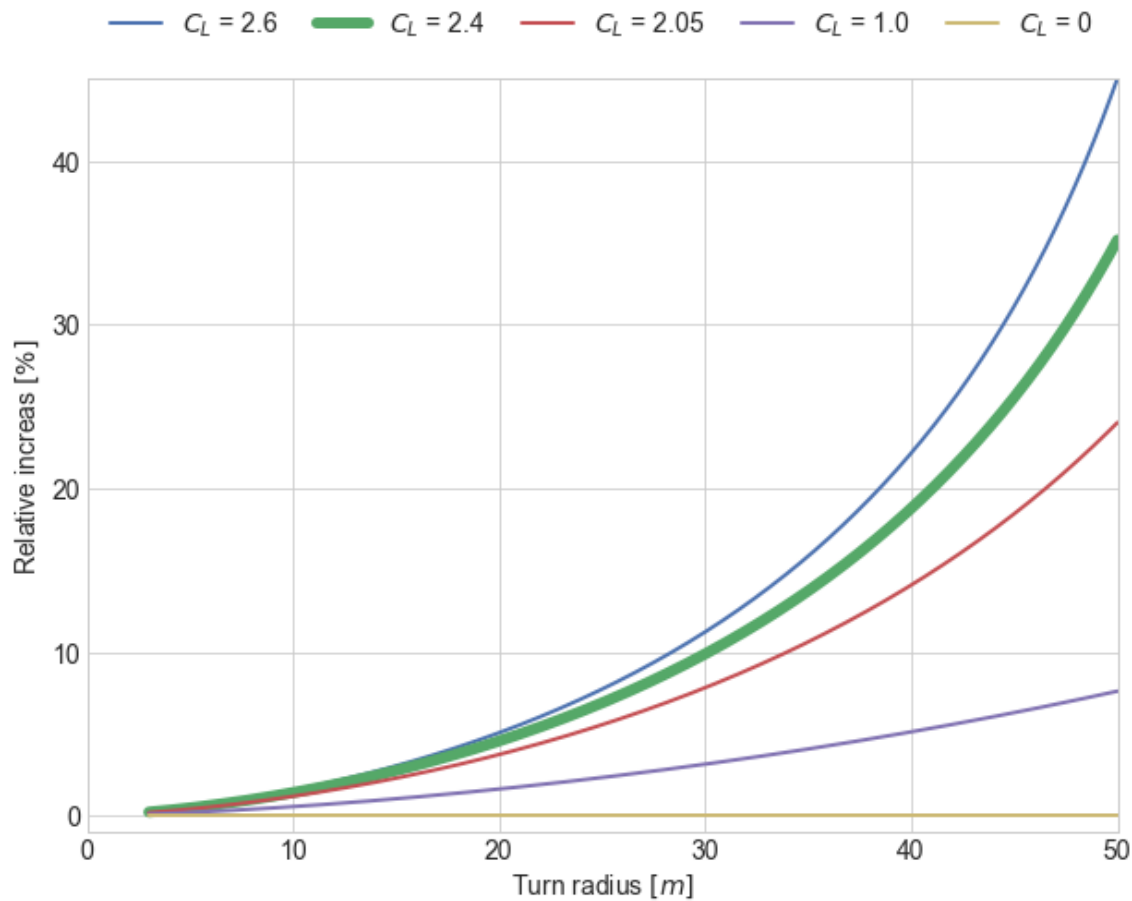


Figure 8.1: Cornering speed as a function of turn radius for various lift coefficients, relative to a  $C_L = 0$ .

# 9

## Conclusion

Vermilion Racing's rear wing has been designed based on initial research, wind tunnel experiments and simulations. Each step has been fundamental to the understanding of the importance of the theory, and will serve as a tool for future generations to expand upon.

The rear wing's dimensions are restricted by the rules of the competition, and serve as the boundaries of the design, giving us the width and height of the wing. The wing's airfoils are chosen based on XFOIL simulations of lift profiles. Due to the nature of the competition, a highly stable wing is wanted - stalling is fatal to the car's handling abilities, which is why the highly cambered MSHD airfoil was chosen. Increasing the amount of elements greatly increases the possible angles of attack, and based on theory and time constraints, a two-element wing with identical airfoils serves as the best opportunity for increasing the lift.

The initial concept was tested in a wind tunnel on a quarter scale model, where the results were compared to simulations. An irregularity in the results instigated further examination of the scale model, revealing a misplacement of the second wing element. After simulating their relative placement, it was discovered that relative placement is very important for lift. Therefore, new wind tunnel tests should be performed in order to verify the lifting characteristics of the wing.

After simulating and optimizing position, a proposed design was drawn. Metallic inserts in order to reinforce the wing and physically mount it to the end plates were topologically optimized to reduce weight. The final design of the rear wing, combined with initial simulations of the

## 9. Conclusion

---

remainder of the car shows to give a total down force of  $C_L = 2.4$ , which should give an increase in cornering speed of 3 – 35%, based on the cornering radius.

Finally, a series of propositions for improving the rear wing design can be read in chapter 9. Many of these should bring great improvements to the Eevee's lift characteristics.

# Perspective

The Eevee has to be rebuilt next year, and in order to help the effort along for future students, a list of potential upgrades are listed below, with estimates of how valuable each change is in regards to downforce/drag reduction gain.

## 9.1 Drag Reductive System

A drag reductive system (DRS) is well-known from Formula 1, and has in the recent years been gaining traction (or lack therof :))) ) in the Formula Student. It is a natural extension to the aerodynamics of the car, as Formula Student has much less restrictions on aerodynamics than Formula 1. Automatically adaptive DRS, that measures the car's relative downforce and the angle of the steering column could give a big edge on straights, as flipping the wing up to reduce drag increases the top speed.

## 9.2 Slats, Flaps, Gills and Cutaway

We already have a multi element wing, but increasing the amount of elements increases the amount of downforce we can pull out of the same design.

## 9.3 Suspension Integration

Nice to have downforce directly on the wheels, but at the trade off of having more unsprung mass though. That might be an issue.

# List of Figures

1.1	The teams' race car with the conceptual design of the rear wing. . . . .	1
2.1	Frontal area of the car with a dummy wing inserted into the CAD model, in order to get an estimate of the drag coefficient $C_D$ . . . . .	6
2.2	Cornering speed as a function of turn radius for various lift coefficients. . . . .	9
3.1	Figure explaining angle of attack, chord line, camber line, upper surface (suction surface), lower surface (pressure side), leading edge and trailing edge. Figure taken from [8]. . . . .	12
3.2	A figure showing the streamlines around a slightly cambered airfoil, along with its pressure distribution below. Figure taken from [2]. . . . .	13
3.3	The trailing tip vortex is clearly seen to the right. Thanks to the NASA's Wake Vortex Study for the photo [13]. . . . .	16
3.4	Lift coefficient as a function of effective angle of attack. The No slot line corresponds to a single element wing, and the 1 slot corresponds to a double element wing. Figure taken from [2]. . . . .	18
4.1	A comparison of the three airfoils as a function of angle of attack. The MSHD profile shows high lifting characteristics over a wide range of angles of attack. Comparisons are from XFOIL at $Re = 3 \times 10^5$ . . . . .	22
4.2	The ruleset above drawn against the design of the car. The marked square is the area where the wing can be freely placed. . . . .	24
4.3	Initial design of the rear wing based on the PDS and initial research. Optimization of the wing is the next step. . . . .	26

## List of Figures

5.1	Robert Mikkelsen posing in front of the Red wind tunnel. To the left is the air inlet, followed by the test section. . . . .	31
5.2	Blueprints of the centrepiece of the wing containing the pressure taps for generating a pressure distribution profile. . . . .	32
5.4	Pieces of the downscaled wing before assembly. Additional H7 holes had to be drilled in order to mount the wing to the force gauge securely. . . . .	34
5.5	Down-scaled wing assmembled with a zoom in on the pressure taps. The length of the entire wing is approximately 250 mm with a total chord length of 150 mm. . . . .	36
5.6	The lift coefficient plotted as a function of the wing's overall AOA. The wing's own angle of attack is $35^\circ$ , which is beyond the theoretical optimum as seen in figure 4.1. . . . .	37
5.7	The upper end plate can be seen deflecting slightly downward due to the lower pressure between the endplates. . . . .	39
6.1	Normalized downforce as a function of mesh size. Plotted to see the convergence towards the same force. . . . .	43
6.2	Surface pressure readout from the 15 pressure taps located on the model at wind speed $40 \text{ m s}^{-1}$ in the wind tunnel. Pressure readout is meand over 3000 measurements and shown with errorbars representing the standard deviation of the measurements. . . . .	44
6.3	2D cut through of the volume mesh used for simulations of the wind tunnel test. Mesh size is approximately $0.4 \cdot 10^7$ cells. . . . .	45
6.4	Monitor of the convergence of the downforce over the number of iterations in Star-CCM+, here shown for a wind velocity of $40 \text{ m s}^{-1}$ . . . . .	45
6.5	Scalar view of the pressure distribution surrounding the two elements of the wing, here at a wind velocity of $40 \text{ m s}^{-1}$ . . . . .	45
6.6	Vector view of the wind velocity surrounding the wing, here at a wind velocity of $40 \text{ m s}^{-1}$ . . . . .	46
6.7	Simulated surface pressure on both elements of the wing. To the left: the larger elements surface pressure and to the right the smaller elements surface pressure is shown. Simulated at wind velocity of $40 \text{ m s}^{-1}$ . . . . .	47
6.8	Comparison of simulated and test found $C_p$ values at a wind velocity of $40 \text{ m s}^{-1}$ . . . . .	48

## List of Figures

---

6.9	Visualization by streamlines of the simulated airflow around the wing. Vortex generation at the rear of the wing is visible.	49
6.10	Optimization of the two element wing. The redder the dots, the higher the lift coefficient.	50
7.1	Cambridge Engineering Selector (CES) showing the various aerospace grade materials usable for this application. The dark red dots are composites, while the dark purple dots are metals such as aluminium and magnesium.	53
7.2	Render of the final design of the rear wing in exploded view.	55
7.3	The result of the topology optimization for the large insert, with a weight reduction at about 50 %.	56
7.4	Optimized mesh overlayed on model so excess material could be easily removed.	56
7.5	Render of the final model for the metal insert, with a weight reduction around 40 %.	56
7.6	The hot wire melts the styrofoam while sliding along the wooden template.	58
7.7	Steffan and Nicolai performing a hand layup of the carbon fiber mats around a polystyrene foam core.	59
7.8	Curing the wing in a flat position lets the resin pool in the center of the wing. This causes the surface to be very rough, potentially causing the boundary layer to trip early. A very unwanted effect that requires mending.	60
7.9	Sanding the wing clears the surface roughness, but requires a new layer of sealant. Using epoxy or a lacquer was investigated before settling on epoxy.	61
8.1	Cornering speed as a function of turn radius for various lift coefficients, relative to a $C_L = 0$ .	66
A.1	Picture of the LabVIEW program used to receive data	74

# A

## Appendix

The following section contains the appendix. However, the entirety of the project, along with figures, code and simulations is found on [https://github.com/carlegroen/bachelor\\_project\\_racecar\\_aero](https://github.com/carlegroen/bachelor_project_racecar_aero), and the reader is referred hereto.

## A. Appendix

---

### Appendix A:LabVIEW program

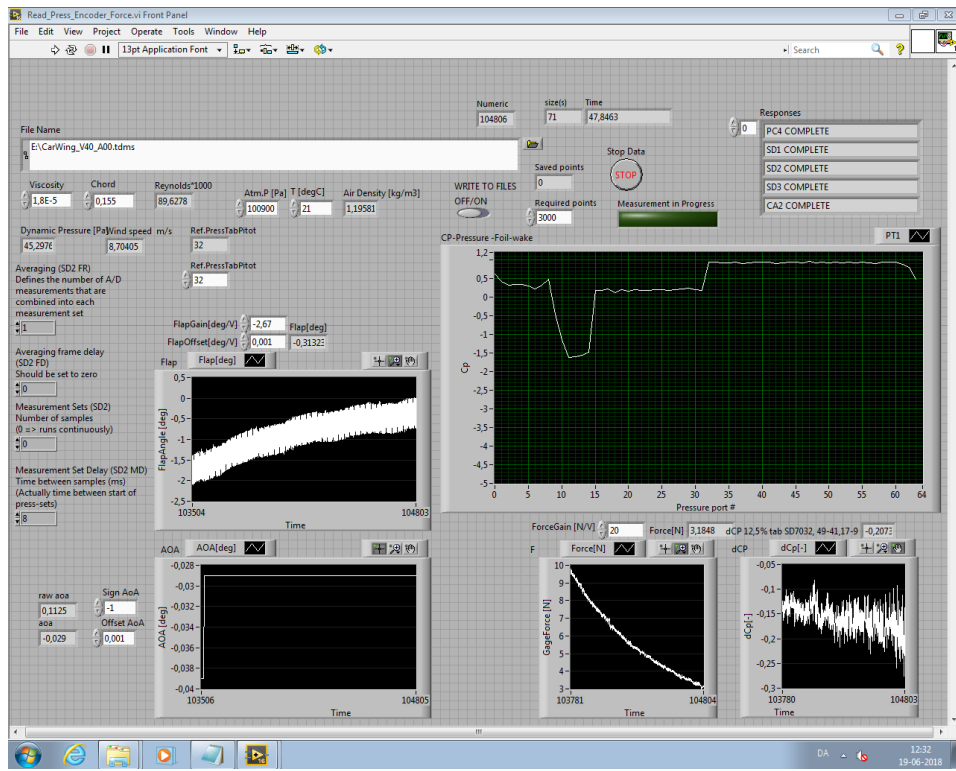


Figure A.1: Picture of the LabVIEW program used to receive data

# Bibliography

- [1] Bulbapedia. <http://bulbapedia.bulbagarden.net/wiki/Eevee>, may 2016.
- [2] Joseph Katz. Race Car Aerodynamics. BentleyPublishers, 2nd edition, 2003.
- [3] J.R. Taylor. Classical Mechanics. University Science Books, 2005.
- [4] IMechE: Institution of Mechanical Engineers. Formula Student Rules. 2018.
- [5] lcdesign. Formula sae aerodynamics. <https://sites.google.com/site/lcdesignwork/case-studies/automotive-case-studies/formula-sae>.
- [6] HPWizard. Tire friction and rolling resistance coefficients. <http://hpwizard.com/tire-friction-coefficient.html>.
- [7] Hucho W. Aerodynamics of road vehicles. Warrendale, 4th edition, 1998.
- [8] Olivier Cleynen. Airfoil nomenclature. [https://en.wikipedia.org/wiki/Airfoil#/media/File:Wing\\_profile\\_nomenclature.svg](https://en.wikipedia.org/wiki/Airfoil#/media/File:Wing_profile_nomenclature.svg).
- [9] NASA. The lift coefficient. <https://www.grc.nasa.gov/www/K-12/airplane/liftco.html>, 2015.
- [10] Joseph Katz and Allen Plotkin. Low-Speed Aerodynamics. Cambridge Aerospace Series. Cambridge University Press, 2 edition, 2001.
- [11] NASA. The lift coefficient. <https://www.grc.nasa.gov/www/K-12/airplane/dragco.html>, 2015.

## Bibliography

---

- [12] NASA. Induced drag coefficient. <https://www.grc.nasa.gov/www/k-12/airplane/induced.html>.
- [13] NASA Langley Research Center. Vortex created by the passage of an aircraft wing. [https://en.wikipedia.org/wiki/Vortex#/media/File:Airplane\\_vortex\\_edit.jpg](https://en.wikipedia.org/wiki/Vortex#/media/File:Airplane_vortex_edit.jpg).
- [14] Peter Kämpf. Lift creation and induced drag. <https://aviation.stackexchange.com/questions/8556/is-a-winglet-better-than-an-equal-span-extension/8579#8579>.
- [15] Tom Benson. The lift coefficient. <https://www.grc.nasa.gov/www/k-12/VirtualAero/BottleRocket/airplane/kitedown.html>.
- [16] P.S. Sriram, Ashok Gopalarathnam, and Andrew Misenheimer. High-downforce airfoil design for motorsports, 2012.
- [17] R.H. Barnard. Road Vehicle Aerodynamic Design: An Introduction. MechAero, 2001.
- [18] Dan Harmon Justin Roiland. [https://youtu.be/w-wbWGwZ7\\_k?t=43s](https://youtu.be/w-wbWGwZ7_k?t=43s), 2017.
- [19] G Savage. Composite materials technology in formula 1 motor racing. Honda Racing F1 Team, 91:92, 2008.
- [20] Bo Madsen Christian Malte Markussen, Tom Løstrup Andersen. Introduction to Vacuum Infusion Molding. 2016.
- [21] Bjarne Chr. Jensen. Teknisk Ståbi. 24 edition, 2015.
- [22] Lacquer surfaces vs. resin surfaceswhats the difference? <https://kinon.com/lacquer-surfaces-resin-surfaces-whats-the-difference>, 2018.
- [23] Viggo Tvergaard. Styrkelære: Statik og Bjælketeori. Polyteknisk Kompendie, 2010.